DESIGN OF MACHINES AND STRUCTURES

A Publication of the University of Miskolc

Volume 12, Number 1

CONTENTS

USING NUMERICAL SIMULATION TO INVESTIGATE THE EFFECT OF LAYER THICKNESS ON RESIDUAL STRESS AND WARPING OF SPECIMENS MADE OF ABS

HUSSEIN ALZYOD[1] – PETER FICZERE[2]

[1, 2]*Budapest University of Technology and Economics,*
H-1111 Budapest Megyetem rkp.3
[1]*hussein.alzyod@edu.bme.hu,* [2]*ficzere.peter@kjk.bme.hu.*
https://orcid.org/0000-0003-3207-5501 (P. Ficzere)
https://orcid.org/0000-0002-6304-4540 (H. Alzyod)

Abstract: Fused Filament Fabrication (FFF) is an additive manufacturing technology that is used to create a wide range of parts and applications. Along with its benefits, there are some challenges regarding the printed parts' mechanical properties, which are associated with printing parameters like layer thickness, infill density, print speed, and nozzle temperature. Experimentally investigation of these pamperers is costly and time-consuming. Some simulations are available to use the numerical solution in the investigation. This work used Digimat-AM simulation to investigate the effect of layer thickness on the residual stress and warping deformation of printed ABS parts.

Keywords: *Additive Manufacturing, ABS, Residual stress, Warping deformation, Digimat-AM*

1. INTRODUCTION

3D printing, often known as additive manufacturing (AM), produces viable, robust, and permanent parts. One of AM's benefits is that it does not require any specialized or expensive tooling, allowing it to work with various materials [1], [2]. By 2025, the AM market will provide an annual economic impact of $200 billion to 600 billion dollars [3], [4]. 3D printing impacts how items are created and made, and its application will expand in the coming years [5], [6]. Material extrusion (ME) [4] is preferable for polymer AM because of its low cost and simplicity of constructing complicated shapes. Since it is a trademark of Stratasys Inc., ME is also known as fused deposition modelling (FDM) or fused filament fabrication (FFF). ME offers a wide range of polymers, both reinforced and unreinforced. Various companies produce and sell 3D printers based on that technology, with varying characteristics such as filament types, accuracy, and printing workspace. In FFF, the material is extruded through a nozzle. That extruded material is a heated filament; then, the material comes out from the nozzle in a molten state to form the layer. It solidifies and binds with outer layers when extruded on the previous layer on the building platform [7]. FFF uses process parameters to print a product, much like any other manufacturing technique. The outcome is

affected by changes in certain operating characteristics. Using diverse AM technologies, researchers investigated the influence of 3D printing parameters on various reactions like printing orientation, printing pattern, nozzle temperature, printing speed [8]–[13]. Samples are formed of polylactic acid (PLA), acrylonitrile–butadiene–styrene (ABS), polyamide (PA) 6 and 12, a combination of PC and ABS, polycarbonate (PC), polyether-ether-ketone (PEEK), or polyetherimide (PEI).

The relationship between printing parameters and mechanical characteristics is determined by many types of testing like compression, torsion, tensile. The FFF technique also produces manufacturing time and the accuracy dimension of the printed part as output variables. Researchers have chosen a simulation to make a numerical solution to investigate different ME factors in plastic materials, with various goals and objectives. One proposal is to study the manufacturing process solely from the standpoint of material deposition, neglecting the mechanical characteristics of the printed parts. A further approach is to analyze the mechanical properties of 3D printed samples using simulations that do not duplicate the material extrusion process but change the printing parameters such as layer thickness, infill density, print speed, and nozzle temperature.

Residual stress is a result of plastic materials' ME. It changes the mechanical characteristics of specimens and should be considered for further research into AM components Studies related to residual stresses fully understand simulations that anticipate them. After that, the part's mechanical properties are calculated, considering the residual stresses that have built up during the printing process. Softwares such as Abaqus, Digimat, and ANSYS are used to generate computational models. ABS, PLA, nylon, and polyphenylene sulfide (PPS) are common materials. Printing parameters are changed to predict the magnitude and position of residual stresses. Various types of heat transfer occur during printing when materials are extruded and deposited. The most important is the heat exchange with the environment via convection and conduction between neighbouring layers and machine support [14]. Thermal history is associated with the formation of residual thermal stresses, which affect component dimensional precision and mechanical behaviour [15], [16]. Changes in the temperature profile of AM parts during the production process could cause problems. The molten material is deposited on a building platform at a high temperature, generating a fast cooling rate that impacts the part's mechanical characteristics [17]. The present paper investigates the effect of layer thickness on the residual stress and warping deformation using Digimat-AM software.

2. Simulation procedures

The simulation process starts with a 3D modelling design created with Solid Edge software. Solid Edge is commonly utilized in various industries, including architecture, manufacturing, electronics, and aerospace. Solid Edge 3D software includes several outstanding features, such as the wide range of platforms available in the

mechanical engineering sector, which allows for the creation of unique design aspects. A three-dimensional cuboid prototype was created (in STL format) with 100 mm long, 100 mm depth, and 5 mm thickness, as shown in *Figure 1*.
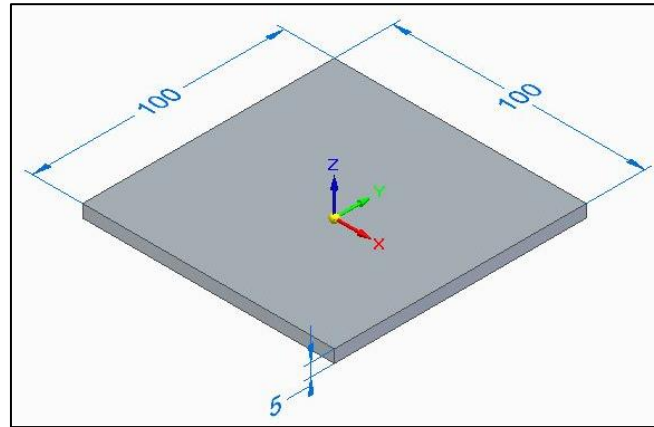
Figure 1. *The 3D shape of the specimen*

The STL (Standard Triangle Language) file type is transformed into printing commands of thin layers using slicer software like Ultimaker Cura or Slic3r, creating a G-Code (G-Programming Language) file containing all orders and instructions such as layer thickness, printing path, and printing orientation. The printing path of the designed specimen is +45°/–45°, as shown in *Figure 2*.
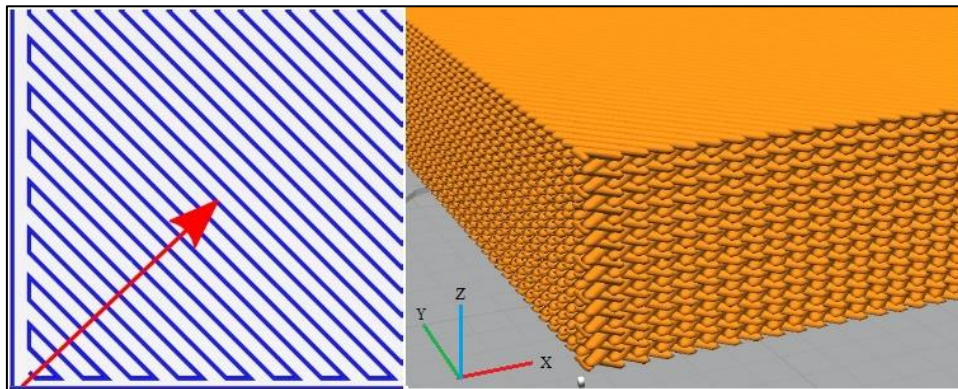
Figure 2. *Printing pattern +45°/–45°*

The STL file and G-Code file are used in Digimat-AM software. Digimat-AM simulates different types of polymers and composites, and it provides a prediction of warpage and residual stresses of a printed part. Digimat-AM software has a workflow that is illustrated in *Figure 3* [18].
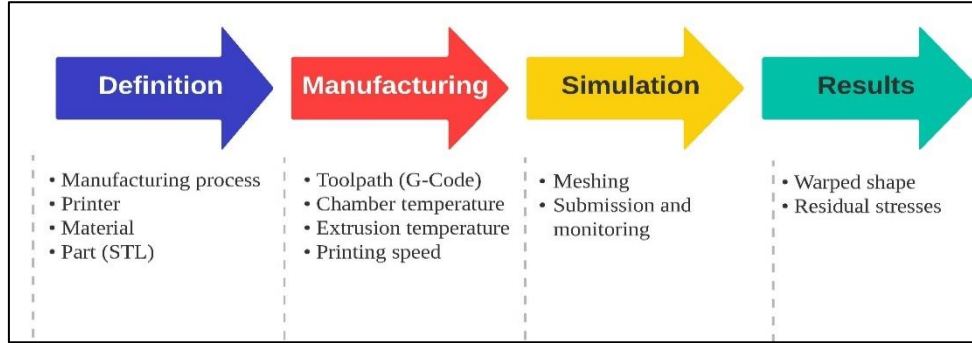
***Figure 3.** Digimat-AM workflow* [18]

In the definition step, the FFF manufacturing process is selected with a generic FFF printer with a chamber size of 200 × 200 × 200 mm and a fixed platform. The ABS material is chosen from the Digimat database. Then the geometry is imported using the STL file. The process parameters are defined in the manufacturing stage. For this investigation, the parameters are illustrated in *Table 1*. The toolpath of printing is determined using a G-Code file.

Table 1
Process parameters for simulation

Process parameter	Value	Unit
Chamber temperature	30	°C
Extrusion temperature	250	°C
Room temperature	23	°C
Printing speed	60	mm/s
Final temperature	23	°C

Finally, in the simulation step, the geometry has meshed then, the job is submitted to get the results. In this study, four simulations were done with different layer thicknesses. The chosen layer thickness was 0.19 mm, 0.29 mm, 0.39 mm, and 0.49 mm.

3. RESULTS AND DISCUSSION

Table 2 shows the results of the simulation with different layer thicknesses. *Figure 4* demonstrates the results of residual stresses and warping deformations of a printed part with a layer thickness of 0.29 mm in the Digimat-AM simulation.

Table 2
Results of residual stress and warping deformation with different layer thicknesses

Layer thickness[mm]	Residual stress [MPa]	Warping deformation [mm]
0.19	5.025	1.522
0.29	2.683	1.525
0.39	1.102	1.473
0.49	0.207	1.445
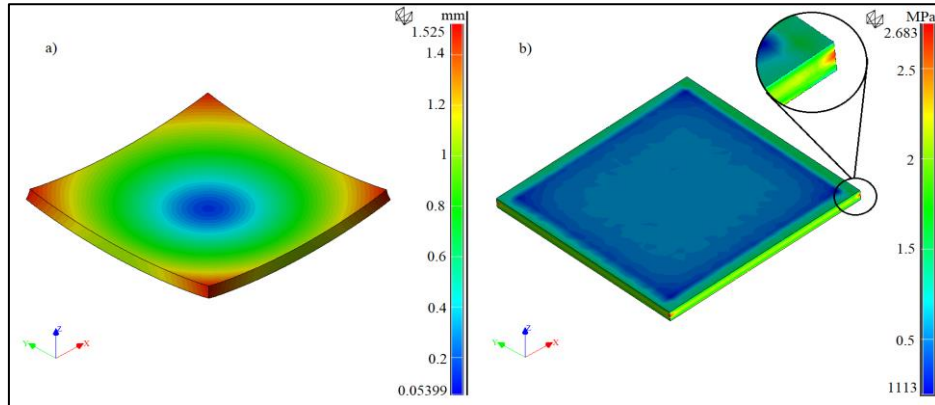
Figure 4. *Results provided by Digimat-AM for 0.29 mm layer thickness:*
a) the warping deformation, b) the residual stress (von Mises)

As shown in *Figure 5*, there is a negative correlation between the layer thickness and the residual stress. The mean residual stress was 2.25 ±1.05 MPa. While there is no correlation between the layer thickness and the warping deformation, as shown in *Figure 6*. The mean of warping deformation was 1.49 ±0.019 mm.
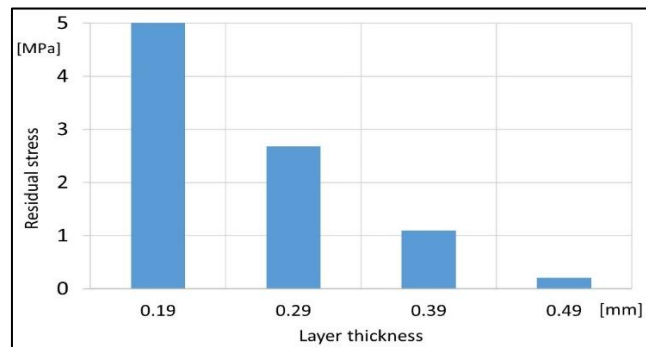
Figure 5. *The relation between layer thickness and residual stress*
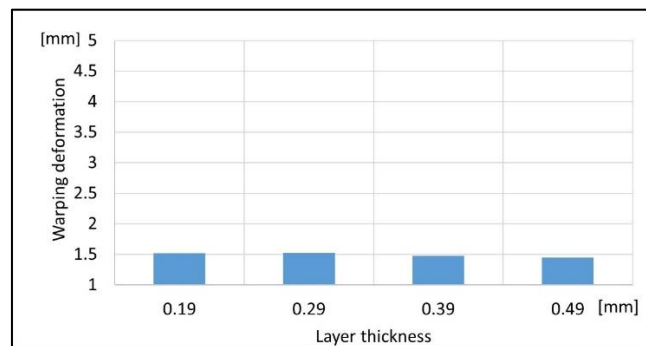
Figure 6. *The relation between layer thickness and warping deformation*

4. CONCLUSIONS

The present work used numerical simulation to investigate the impact of layer thickness on residual stress and warping deformation of 3D printed parts made of ABS material. The results showed a significant negative correlation between the layer thickness and the residual stress. Meanwhile, the warping deformation did not change by changing the layer thickness. The total warping deformation is relatively high with respect to the entire thickness of the part. This warping is extremely higher than the layer thickness, which may lead to failure in the physical printing due to collusion between the part and the printing nozzle.

REFERENCES

[1] Alaimo, G. – Marconi, S. – Costato, L. – Auricchio, F. (2017). Influence of meso-structure and chemical composition on FDM 3D-printed parts. *Composites Part B: Engineering*, Vol. 113, March, pp. 371–380. https://doi.org/10.1016/j.compositesb.2017.01.019

[2] Conway, K. M. – Pataky, G. J. (2019). Crazing in additively manufactured acrylonitrile butadiene styrene. *Engineering Fracture Mechanics*, Vol. 211, Apr., pp. 114–124, https://doi.org/10.1016/j.engfracmech.2019.02.020.

[3] Disruptive technologies: Advances that will transform life, business, and the global economy. *McKinsey*, https://www.mckinsey.com/business-functions/mckinsey-digital/our-insights/disruptive-technologies# (accessed Feb. 22, 2022).

[4] Ficzere, P. (2022). The Impact of the Positioning of Parts on the Variable Production Costs in the Case of Additive Manufacturing. *Periodica Polytechnica Transportation Engineering*, Feb., https://doi.org/10.3311/PPtr.15827.

[5] Alsardia, T. – Lovas, L. – Ficzere, P. (2021). Prototype for fit investigations. *Design of Machines and Structures*, Vol. 11, No. 1, pp. 5–15. https://doi.org/10.32972/dms.2021.001

[6] Ficzere, P. – Lukács, N. L. (2020). The possibilities of intelligent manufacturing methods. *Design of Machines and Structures*, Vol. 10, No. 1, pp. 13–19. https://doi.org/10.32972/dms.2020.002

[7] Rashid, A. (2019). Additive Manufacturing Technologies. *CIRP Encyclopedia of Production Engineering*, pp. 1–9. https://doi.org/10.1007/978-3-642-35950-7_16866-1

[8] Ding, S. – Zou, B. – Wang, P. Ding, H. (2019). Effects of nozzle temperature and building orientation on mechanical properties and microstructure of PEEK and PEI printed by 3D-FDM. *Polymer Testing*, Vol. 78, Sept. p. 105948. https://doi.org/10.1016/j.polymertesting.2019.105948

[9]   Wankhede, V. – Jagetiya, D. – Joshi, A. – Chaudhari, R. (2020). Experimental investigation of FDM process parameters using Taguchi analysis. *Materials Today: Proceedings*, Vol. 27, Jan., pp. 2117–2120. https://doi.org/10.1016/j.matpr.2019.09.078

[10]   Yao, T. – Deng, Z. – Zhang, K. – Li, S. (2019). A method to predict the ultimate tensile strength of 3D printing polylactic acid (PLA) materials with different printing orientations. *Composites Part B: Engineering*, Vol. 163, Apr., pp. 393–402, https://doi.org/10.1016/j.compositesb.2019.01.025.

[11]   Markiz, N. – Horváth, E. – Ficzere, P. (2020). Influence of printing direction on 3D printed ABS specimens. *Production Engineering Archives*, Vol. 26, No. 3, Sept., pp. 127–130, https://doi.org/10.30657/PEA.2020.26.24.

[12]   Mohamed, O. A. – Masood, S. H. – Bhowmik, J. L. (2016). Optimization of fused deposition modeling process parameters for dimensional accuracy using I-optimality criterion," Measurement, vol. 81, pp. 174–196, Mar. 2016. https://doi.org/10.1016/j.measurement.2015.12.011.

[13]   Raut, S. – Jatti, V. S. – Khedkar, N. K. – Singh, T. P. (2014). Investigation of the Effect of Built Orientation on Mechanical Properties and Total Cost of FDM Parts. *Procedia Materials Science*, Vol. 6, Jan., pp. 1625–1630. https://doi.org/10.1016/j.mspro.2014.07.146.

[14]   Costa, S. F. – Duarte, F. M. – Covas, J. A. (2017). Estimation of filament temperature and adhesion development in fused deposition techniques. *Journal of Materials Processing Technology*, Vol. 245, July, pp. 167–179. https://doi.org/10.1016/j.jmatprotec.2017.02.026.

[15]   Quelho de Macedo, R. – Ferreira, R. T. L. – Jayachandran, K. (2019). Determination of mechanical properties of FFF 3D printed material by assessing void volume fraction, cooling rate and residual thermal stresses. *Rapid Prototyping Journal*, Vol. 25, No. 10, Nov., pp. 1661–1683. https://doi.org/10.1108/RPJ-08-2018-0192/full/pdf.

[16]   Alhafadhi, M. – Krállics, G. (2020). Effect of the welding parameters on residual stresses in pipe weld using numerical simulation. *Design of Machines and Structures*, Vol. 10, No. 1, pp. 5–12, https://doi.org/10.32972/dms.2020.001.

[17]   Savane, V. – Hansen, C. (2017). *Finite Element Simulation of the Fused Deposition Modelling Process Composites simulation View project Multi-scale Material Modeling View project*. Online. Available: https://www.research gate.net/publication/313819691.

[18]   Hebert, P. – Lietaer, O. (2017). New developments in simulation for plastics & metals: Multiscale Modeling of AM Process of Plastics & Composites. *MSC Software Magazine*, pp. 12–16. [Online]. Available: www.mscsoftware.com/event4.

CALCULATION OF THE FLOW GENERATED
IN THE RUNNER OF A BÁNKI TURBINE

SÁNDOR HAJDÚ

University of Miskolc, Institute of Energy Engineering and Chemical Machinery
3515 Miskolc-Egyetemváros
hajdus1@outlook.hu

Abstract: The article describes the numerical calculation of a streamline in a liquid jet flowing through the impeller of a Bánki turbine. The importance of the results summarized in the article is that the knowledge of the velocity situation in the liquid jet flowing through the impeller is essential for the calculation of the flow losses occurring in the runner of a Bánki turbine and of the hydraulic efficiency of the runner.

Keywords: streamline, methodology, Bánki turbine

1. INTRODUCTION

The Hungarian literature of Bánki turbines has been lacking any improvement of the theory – that has remained the same since the age of Bánki – for a long time. In order to reach any advancement, a completely new way, which diverges from the previously available literature on Bánki turbines, had to be found in the research work. An important partial result of this new way is a new procedure of calculating the physical properties of the flow generated in the runner of a Bánki turbine, the flow losses in the runner of a Bánki turbine, and the hydraulic efficiency of the runner.

2. THE BÁNKI TURBINE

The Bánki turbine utilizes the kinetic energy of the mass flow of the liquid flowing through it. The theoretical head of the runner is equal to the drop in the kinetic energy of the liquid flowing through the runner, related to the unit liquid mass. The liquid fills only a part of the turbine runner. The blade force generated by the interaction between the blades and the liquid diverts the jet. The rotational speed of the runner is determined by the balance of the shaft torque (driving the generator) and the torque generated by the blade force that diverts the jet.

The liquid enters the runner of a Bánki turbine as a free jet. The pressure in a free jet is equal to the environmental pressure. The velocity of the free jet is determined by the available head drop, which means that the quantity of liquid that flows through the runner of a Bánki turbine through unit time is independent of the rotational speed of the runner.

The volumetric flow rate of the liquid that enters the runner is the product of the velocity component perpendicular to the entry surface and the size of the entry surface. The liquid that exits from the guiding channel *(Figure 1)* flows through the blade set of the runner *transversally*, i.e. the entry and the exit surfaces of the liquid are identical. The liquid arriving at the runner circumference flows through the blade set in the *centripetal* direction at first, and then, after passing through the bladeless part inside the runner, enters the blade set again, and flows through it in the *centrifugal* direction before leaving it.

The blade curve has a circular arc shape [2], [3]; the tangents of the blade curve are radial along the inside edge of the bladed area.
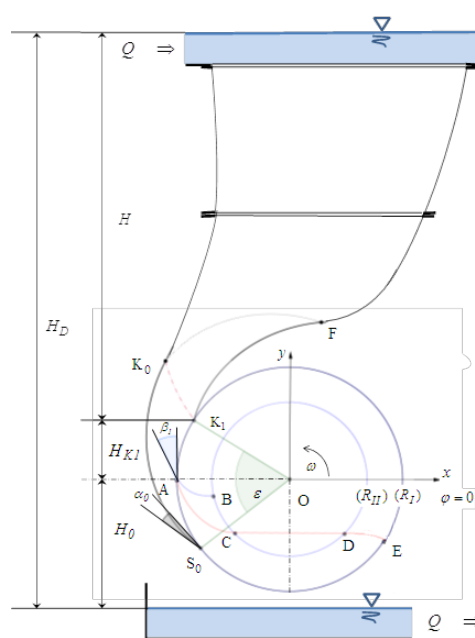
Figure 1. *Schematic of a Bánki turbine*

The directrix of the guide channel surface is, with the symbols of *Figure 1*, the curve section K_0S_0 , while that of the movable guide channel surface – i.e. of the regulation flap – in the fully open state is the curve segment K_1F. The directrix of the movable guide channel surface – i.e. of the regulation flap – in the completely fully closed state is the curve section K_0F.

The direction angle of the flow entering the runner is the angle between the tangent of the guide channel and that of the circle with the radius R_I , i.e. α_0 . This angle is constant along the runner circumference involved in the liquid entry (K_1S_0). Bánki ensured this by constructing the cylinder-like K_0S_0 and FK_1 surfaces of the guide channel, which are situated between two parallel planes, in a way that their

directrices be logarithmic spirals shifted along the circumference of the runner whose angle of inclination is α_0. The highest available head *(Figure 1)* is:

$$H = H_D - H_0 - H_{K1} = H_D - H_0 - R_I \sin(\varphi_{S0} - \varepsilon) \tag{1}$$

3. CALCULATION OF THE FLOW GENERATED IN THE RUNNER

A complete absolute streamline along the runner consists of three sections from the entry into the runner *(Figure 1)*: the streamline section AC with a centripetal flow direction, the straight streamline CD along the bladeless inside part of the runner and the streamline section DE with a centrifugal flow direction.

Explanation of the indices: the index of velocity and directional angle at the centripetal entry into the bladed runner area is *1;* the index of velocity and directional angle at the centripetal exit from the bladed runner area is *2;* the index of velocity and directional angle at the centrifugal entry into the bladed runner area is *3*; the index of velocity and directional angle at the centrifugal exit from the bladed runner area is *4*.

The origins of the Cartesian coordinate system x, y and of the polar coordinate system r, φ are both located in the centre of the runner, O; the x axis of the Cartesian coordinate system x, y is horizontal. The polar angle φ increases in the counterclockwise direction. The relation between the r, φ polar and the x, y Cartesian coordinates is:

$$x = r \cos\varphi \quad ; \quad y = r \sin\varphi$$
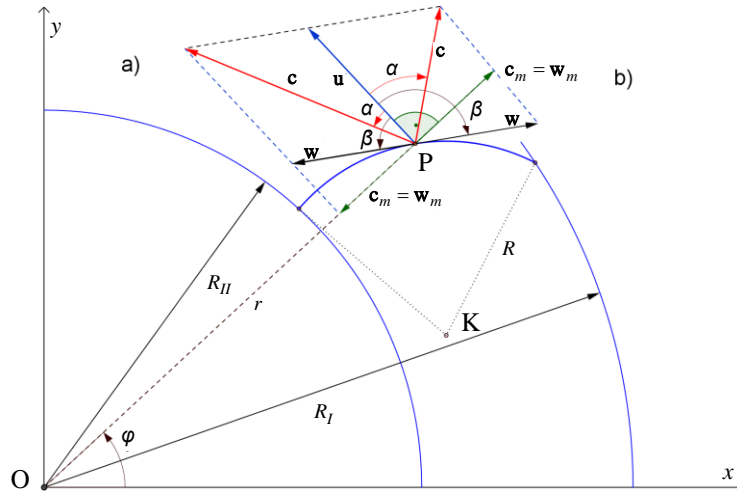
Figure 2
Velocity triangles in one point of the blade curve
a) along the centripetal section
b) along the centrifugal section
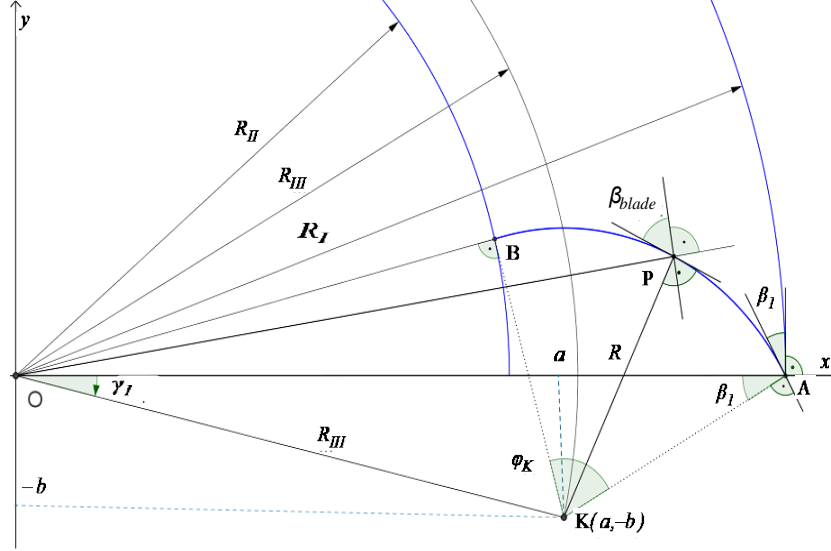
Figure 3. *Geometry of a circular blade arc*

Figure 2 shows a velocity triangle that applies to a random P point in the bladed area of a Bánki turbine, which is situated on a circle of a radius $R_{II} \leq r \leq R_I$, assuming *infinitely dense and infinitely thin blades*, where the relative flow in the bladed area of the runner is *blade congruent*, i.e. the relative streamlines are identical with the blade curves, which means that the relative velocity vectors are identical with the tangents of the blade curves.

Along the circle with the radius of $R_{II} \leq r \leq R_I$ (the index m here and hereinafter refers to the meridian velocity component)

$$c_m = w_m \tag{2}$$

i.e. along a circle of the same radius, *at the centrifugal- and centripetal-flow sections, the relative velocity vectors* **w** *have the same magnitude, but opposite directions (Figure 2)*.

The directional angle β of the relative flow
– along the *centripetal section*: $\beta_1 < \beta \leq \pi/2$ (acute angle);
– along the *centrifugal section*: $\pi/2 \leq \beta \leq \pi - \beta_1$ (obtuse angle).

If assuming a blade congruent relative flow, the outermost streamlines are identical in the jet generated inside the bladed area, which means that the shapes of the outermost streamlines can be rotated around the centre of the runner to cover each other, i.e. the ε angle is constant along the r radius. This means that the theorem of continuity for an incompressible liquid in the bladed area of the runner is described by the equation

$$r c_m = R_I c_{1m} \tag{3}$$

The absolute velocity at the runner entry is defined by the available head H as described by the *Equation (1):*

$$c_1 = \sqrt{2gH} \tag{4}$$

In the bladed runner area, the relation between circumferential velocity u and meridian velocity c_m is the following:

$$u = c_m(\cot\alpha - \cot\beta)$$

(Figure 2). Given the continuity *Equation (3)* and that $u = r\omega = ru_1/R_I$, the above equation can take the following form:

$$u_1\frac{r}{R_I} = \frac{R_I}{r}c_{1m}(\cot\alpha - \cot\beta) \tag{5}$$

Based on the publication of Czibere [1], the operating state of the runner can, using the velocity relation

$$\psi = \frac{u_1}{c_{1m}} \tag{6}$$

be described by the following form of *Equation (5)*:

$$\cot\alpha = \psi\left(\frac{r}{R_I}\right)^2 + \cot\beta \tag{7}$$

which is the *basic equation* of the flow occurring in the bladed area of the runner of a Bánki turbine. This basic equation – assuming a *blade congruent* relative flow – provides a relation between the directional angle α of the absolute flow and that of the relative flow, β, depending on the operating state of the turbine. The basic *Equation (7)* can be used for calculating a streamline of the liquid jet occurring in the runner.

The blade angle β_{blade} is an acute angle in a point P of the blade curve, between the tangent of the circular arc-shaped blade curve and the tangent of a circle concentric with the runner circumference and containing the point P *(Figure 3)*. When assuming a blade congruent relative flow, the directional angle β of the relative velocity in the bladed area of the runner is, along the section with *centripetal* flow, $\beta = \beta_{blade}$ (acute angle), while along the section with *centrifugal* flow, $\beta = \pi - \beta_{blade}$ (obtuse angle). The basic *Equation (7)* of the flow in the bladed area of the runner of a Bánki turbine takes the following form when written with the *blade angle*:

$$\cot\alpha = \psi\left[\frac{r}{R_I}\right]^2 \pm \cot\beta_{blade}(r) \tag{8}$$

where the positive sign applies to the centripetal-flow section ($\beta = \beta_{blade}$), and the negative one to the centrifugal-flow one ($\beta = \pi - \beta_{blade}$).

The angle β_{blade} between the tangent of the circular arc shaped blade curve and the tangent of the circle of a radius r is defined by the following equation based on *Figure 3*:

$$\beta_{blade}(r) = \pi - \arccos\left(\frac{R_{III}^2 - R^2 + r^2}{2r\,R_{III}}\right) - \arccos\left(\frac{R_{III}^2 + R^2 - r^2}{2R_{III}R}\right) \;;\; R_{II} \leq r \leq R_I,$$
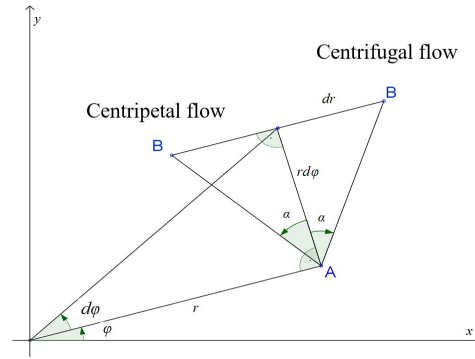
Figure 4. *The relationship between the directional angle α of the absolute velocity and the elementary triangle defined by the differentials*

Along the blade curve, the directions of the relative velocity along the centripetal-flow and the centrifugal-flow sections are opposite, i.e. the differential equations of the streamline parts corresponding to the bladed areas are, in the polar coordinate system r, φ around the rotational axis, different for the centripetal-flow and the centrifugal-flow sections.

Along the *centripetal-flow section,* the relationship between the directional angle α of the absolute velocity and the differentials applying to the elementary AB section of the streamlines can, according to *Figure 4*, be defined using the basic *Equation (8)*:

$$\cot\alpha = -r\frac{d\varphi}{dr} = \psi\left(\frac{r}{R_I}\right)^2 + \cot\beta_{blade}(r)$$

The differential equation of the absolute streamline along the centripetal-flow area is:

$$\frac{d\varphi}{dr} = -\frac{1}{r}\left[\psi\left(\frac{r}{R_I}\right)^2 + \cot\beta_{blade}(r)\right]$$

By integrating it:

$$\varphi(r) = \int_r^{R_I}\left[\psi\left(\frac{r}{R_I}\right)^2 + \cot\beta_{blade}(r)\right]\frac{dr}{r} \quad R_{II} \leq r \leq R_I \tag{9}$$
;

The point of the centripetal section of the streamline, which is located on the runner circumference has, due to $\varphi(R_I) = 0$, the polar coordinates $(R_I; 0)$.

Along the *centrifugal-flow section,* the relationship between the directional angle α of the absolute velocity and the differentials applying to the elementary AB section of the streamlines can, according to *Figure 4*, be defined using the basic *Equation (8)* as written with the blade angle β_{blade}:

$$\cot\alpha = r\frac{d\varphi}{dr} = \psi\left(\frac{r}{R_I}\right)^2 - \cot\beta_{blade}(r)$$

The differential equation of the absolute streamline along the centrifugal-flow area is:

$$\frac{d\varphi}{dr} = \frac{1}{r}\left[\psi\left(\frac{r}{R_I}\right)^2 - \cot\beta_{blade}(r)\right]$$

By integrating it:

$$\varphi(r) = \varphi_D + \int_{R_{II}}^{r}\left[\psi\left(\frac{r}{R_I}\right)^2 - \cot\beta_{blade}(r)\right]\frac{dr}{r} \qquad R_{II} \leq r \leq R_I \tag{10}$$

In the *Equation (10)* the angular coordinate φ_D of the streamline point D depends on the position of the straight streamline part CD *(Figure 5)*. The angular coordinate φ_C of the point C is calculated using the definite integral from *(9)*.

$$\varphi_C = \varphi(R_{II}) = \int_{R_{II}}^{R_I}\left[\psi\left(\frac{r}{R_I}\right)^2 + \cot\beta_{blade}(r)\right]\frac{dr}{r} \tag{11}$$

The direction of the straight streamline section is defined by the directional angle of the streamline in the point C , α_C. This can be calculated using the form of the basic *Equation (8)*, given that in the point C , the blade angle is $\beta_C = \pi/2$ and thus $\cot\beta_C = 0$:

$$\cot\alpha_C = \psi\left(\frac{R_{II}}{R_I}\right)^2 \qquad \Rightarrow \qquad \alpha_C = \operatorname{arc cot}\left[\psi\left(\frac{R_{II}}{R_I}\right)^2\right]$$

Based on *Figure 5*, the angular coordinate of the point D , φ_D is defined by that of the point C , φ_C and by the directional angle α_C, as follows:

$$\varphi_D = \varphi_C + 2\alpha_C$$
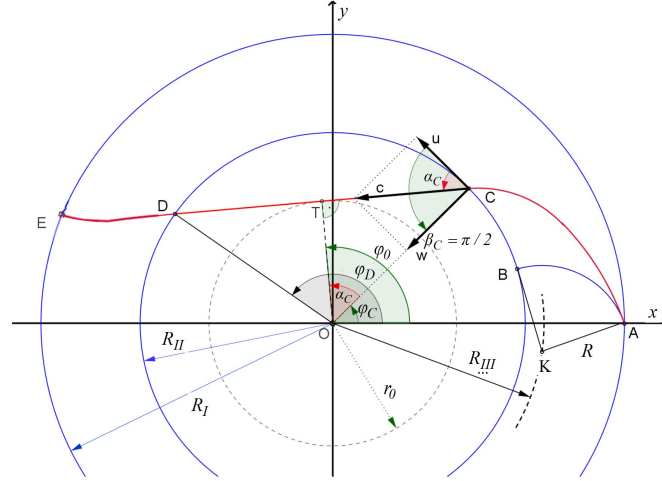
Figure 5. *The shape of an absolute streamline in the runner*

The streamlines at the two outermost points of the water jet arriving at the runner intersect in the bladeless area *(Figure 6)*, which means that the blades force the liquid flow passing through the runner blades centripetally to contract, which results in energy losses. In order to calculate these losses, the approximate shape of the liquid jet occurring in the runner must be determined. The two outermost streamlines of the contracting section of the liquid jet flowing through the runner can be approximated with a circular arc each. These circular arcs touch the outermost streamlines in the points C and D′, resp. **C′** and D along the inside circle of the runner with a radius R_{II} *(Figure 7)*. The cross-sectional ratio of the contracted area of the liquid jet along the circular arc CC' is the ratio of the radius of the jet entering the bladeless area and the smallest radius, b_S / b_k:

$$\frac{A_S}{A_K} = \frac{b_S}{b_K} = \frac{\varepsilon \sin(\varepsilon/2)}{2(1 - \cos(\varepsilon/2))}.$$

The specific energy loss due to the velocity increase caused by the contraction is, related to the unit mass, the following:

$$e'_K = \frac{(c_K - c_2)^2}{2} = \left(\frac{A_S}{A_K} - 1\right)^2 \frac{c_2^2}{2} = \zeta_K \frac{c_2^2}{2},$$

where ζ_K is the contraction loss factor, c_K is the velocity occurring in the cross-section A_K and c_2 is the absolute velocity in the A_S entry cross-section of the contracted jet section, which is identical with the exit velocity into the bladeless area along the cylindrical surface with a radius of R_{II}.

Figure 6. *Streamline sections AC and DE, and their projections A'C' and D'E' as rotated by the central angle ε*

Figure 7. *Contraction of the liquid jet flowing through the blade set*

Given the continuity equation that applies to the centrifugal-flow runner section, $R_{II} c_{2m} = R_I c_{1m}$ the formula

$$c_{1m}^2 = c_1^2 \sin^2 \alpha_0 = c_1^2 \frac{1}{1+\cot^2 \alpha_0},$$

the fact that $\beta_2 = \pi/2$ and thus the basic *Equation (7)* being

$$\cot \alpha_2 = \psi \left(\frac{R_{II}}{R_I} \right)^2$$

in the directional angle α_2, and the formula *(4)*, the following equation can be written:

$$c_2 = \frac{c_{2m}}{\sin \alpha_2} = \frac{c_{1m}}{\sin \alpha_2} \frac{R_I}{R_{II}} = \sqrt{2gH} \frac{\sin \alpha_0}{\sin \alpha_2} \frac{R_I}{R_{II}} = \sqrt{2gH} \frac{R_I}{R_{II}} \sqrt{\frac{1+\psi^2 (R_{II}/R_I)^4}{1+\cot^2 \alpha_0}},$$

and therefore the specific contraction energy loss as related to the unit mass of the flowing medium takes the following form:

$$e'_K = \zeta_K gH \frac{1 + S_{II}^4 \psi^2}{S_{II}^2 (1 + \cot^2 \alpha_0)},$$

where $S_{II} = R_{II}/R_I$ is the runner radius ratio and α_0 is the directional angle of the guide channel. Finally, the power loss of the mass flow ρQ that flows through the runner due to radius contraction is:

$$P'_K = e'_K \rho Q = \zeta_K \rho gQH \frac{1 + S_{II}^4 \psi^2}{S_{II}^2 (1 + \cot^2 \alpha_0)} \tag{12}$$

The frictional losses caused by the *viscosity* of the liquid that flows through the runner of a Bánki turbine occur in the runner blade channels in contact with the medium. The number of blade channels in contact with the flow that enters along the section defined by the central angle ε into a partially open runner with N blades is, along the centripetal-flow section of the blade set, $N\varepsilon/2\pi$, and the same along the centrifugal-flow section, i.e. the total number of blade channels in contact with the medium is $N\varepsilon/\pi$. The length of the rectangular cross-section pipe equivalent to the blade channels in contact with the medium is:

$$L_{cs} = L_k N\varepsilon/\pi,$$

where L_k is the length of the circular arc shaped blade. The relative flow that occurs in the blade channels can be approximated to be a flow in a rectangular cross-section pipe, where the flow velocity is the geometric mean of the relative velocity w_I at the entry into the runner along the circumference of a radius R_I, and the relative velocity w_2 at the exit along the circumference of a radius R_{II}:

$$\overline{w} = \sqrt{w_I w_2} = c_{Im} \sqrt{\frac{R_I}{R_{II} \sin \beta_I}}.$$

The hydraulic diameter of the rectangular cross-section pipe is:

$$D_H = 4\frac{A}{K} = 4\frac{L2\pi R_I/N}{2(L + 2\pi R_I/N)} = \frac{4L\pi R_I}{LN + 2\pi R_I},$$

where A is the cross-section, K is the circumference in contact with the medium, and L is the runner width, which is, in this case, identical with the guide channel width.

The specific *frictional loss* related to the unit mass of the liquid flowing through the runner is:

$$e'_V = \zeta_V \frac{\overline{w}^2}{2} = \zeta_V gH \frac{1}{S_{II} \sin \beta_1 (1 + \cot^2 \alpha_0)},$$

where ζ_V is the frictional loss factor, which can be calculated using the following formula:

$$\zeta_V = \lambda_{cs} \frac{L_{cs}}{D_H} \cdot$$

The pipe friction factor λ can be calculated using the well-known pipe friction law when the Reynolds number $\mathrm{Re} = \overline{w} D_H / \upsilon$ is known. Therefore, the power loss caused by the medium viscosity in a mass flow ρQ is:

$$P_V' = \zeta_V \rho\, gQH \frac{1}{S_{II} \sin \beta_1 (1 + \cot^2 \alpha_0)} \tag{13}$$

The basic *Equation (7)* dictates that the blade angle at the entry, β_1, and the velocity ratio that defines the operating state of the runner, $\psi = u_1 / c_{1m}$ (where u_1 is the tangential velocity in the runner entry point and c_{1m} is the radial component of the entry velocity in the same point) unambiguously define the absolute directional angle α_1 of the entry velocity c_1:

$$\cot \alpha_1 = \psi + \cot \beta_1 .$$

If this directional angle α_1 is identical with the directional angle α_0 of the Bánki turbine guide channel, the absolute flow will enter the runner without any *directional refraction*. This so-called *impact-free* inflow will, according to the previous equation, occur in the

$$\psi_0 = \cot \alpha_0 - \cot \beta_1$$

operating state of the runner. If the turbine operating state is different $(\psi \neq \psi_0)$, the directional angle α_1 of the absolute entry velocity will also differ from the directional angle α_0 of the guide channel – in this case, an energy loss will occur in the liquid jet entering the runner. This specific energy loss, related to the unit mass flow, is proportional to the square of the absolute value of the velocity difference $\Delta \mathbf{c}$ between the absolute velocity at a directional angle $\alpha_1 \neq \alpha_0$ and that at a directional angle α_0 (the latter being the impact-free operating state):

$$e_0' = \zeta_0 \frac{|\Delta c|^2}{2} = \zeta_0 \frac{|u_1 - u_0|^2}{2} = \zeta_0 \frac{(\psi - \psi_0)^2 c_{1m}^2}{2}$$

where ζ_0 is the impact loss factor and c_{1m} is the meridian component of the velocity of the liquid jet entering the runner, which is defined by the available elevation drop H and the directional angle α_0 of the guide channel:

$$c_{1m} = \sqrt{2gH} \, \sin \alpha_0 = \sqrt{\frac{2gH}{1 + \cot^2 \alpha_0}}$$

In the fully open state, the impact-related power loss in a mass flow ρQ through the runner is:

$$P_0' = e_0' \rho Q = \zeta_0 \rho gQH \frac{(\psi - \psi_0)^2}{1 + \cot^2 \alpha_0} \tag{14}$$

The power of the liquid jet arriving at the runner of a Bánki turbine in the fully open turbine state is unambiguously defined by the mass flow ρQ arriving at the runner and the available elevation drop H :

$$P_H = \rho gQH \, .$$

The *theoretical* elevation drop of the runner is, in the fully open turbine state, equal to the change in the kinetic energy of the unit weight of the liquid that flows through the turbine:

$$H_E = \frac{c_1^{\,2} - c_4^{\,2}}{2g} = \frac{c_1^{\,2}}{2g} \left(1 - \frac{c_4^{\,2}}{c_1^{\,2}} \right) \tag{15}$$

Given that $c_1 = \sqrt{2gH}$; $c_{1m} = c_{4m}$; $c_1 = c_{1m}/\sin \alpha_0$; $c_4 = c_{4m}/\sin \alpha_4$ and using the identity $\sin^2 x = 1/(1 + \cot^2 x)$, the velocity ratio c_4 / c_1 can be described by the following formula:

$$\frac{c_4^2}{c_1^2} = \frac{\sin^2 \alpha_0}{\sin^2 \alpha_4} = \frac{1 + \cot^2 \alpha_4}{1 + \cot^2 \alpha_0} \, ,$$

and the basic *Equation (7)* dictates, (given that $\beta_4 = \pi - \beta_1$) that

$$\cot \alpha_4 = \psi + \cot \beta_4 = \psi - \cot \beta_1 \, ,$$

therefore the Equation (15) can be written in the following form:

$$H_E = H \left(1 - \frac{1 + (\psi - \cot \beta_1)^2}{1 + \cot^2 \alpha_0} \right)$$

which means that the theoretical power of the runner is:

$$P_E = \rho gQH_E = \rho gQH \left(1 - \frac{1 + (\psi - \cot \beta_1)^2}{1 + \cot^2 \alpha_0} \right) .$$

By subtracting the impact loss P_O', the contraction loss P_K' and the frictional loss P_V' from the theoretical power P_E of the runner, the runner power P_{jk} is obtained. In the fully open state, the *hydraulic efficiency* of the runner is the ratio of the runner power and the power of the liquid jet arriving at the runner:

$$\eta_{jk} = \frac{P_{jk}}{P_H} = \frac{P_E - (P_0' + P_K' + P_V')}{P_H} =$$

$$= 1 - \frac{1 + (\psi - \cot\beta_1)^2}{1 + \cot^2\alpha_0} - \frac{\zeta_0 S_{II}^2(\psi - \psi_0)^2 + \zeta_K(1 + S_{II}^4\psi^2)}{S_{II}^2(1 + \cot^2\alpha_0)} - \tag{16}$$

$$\left. - \frac{\zeta_V}{S_{II}\sin\beta_1(1 + \cot^2\alpha_0)} \right)$$

The hydraulic efficiency of a stationary runner (in this state, $\psi = 0$) is zero. The freely selectable impact loss factor ζ_0 should be selected so that, in case of $\psi = 0$, the hydraulic efficiency calculated using *(16)* be zero. By multiplying both sides of the equation $\eta_{jk} = 0$ with the expression $1 + (\psi_0 + \cot\beta_1)^2$ – given that the basic *Equation (7)* dictates that $\cot\alpha_0 = \psi_0 + \cot\beta_1$ –, the following equation is obtained to the loss factor ζ_0:

$$\psi_0^2 + 2\psi_0\cot\beta_1 - \frac{\zeta_0\psi_0^2 S_{II}^2 + \zeta_K}{S_{II}^2} - \zeta_V\frac{1}{S_{II}\sin\beta_1} = 0$$

From this equation, the impact loss factor ζ_0 can be written in the following formula:

$$\zeta_0 = 1 + \frac{2\cot\beta_1}{\psi_0} - \frac{\zeta_K}{\psi_0^2 S_{II}^2} - \frac{\zeta_V}{\psi_0^2 S_{II}\sin\beta_1} \tag{17}$$

4. SUMMARY

Assuming a circular arc-shaped blade curve (the tangent to the blade curve is radial at the inside edge of the bladed area) and a blade congruent relative flow, the formulas deduced in the publication make it possible to calculate the r, φ coordinates of the points of a streamline in the free jet crossing the runner from the dimensions R_I, R_{III}, R of a Bánki turbine runner in a required operating state ψ. Based on these coordinates, the complete streamline can be drawn by points in the coordinate plane r, φ. No such calculation has been published in the literature yet. Once the velocity situation in the liquid jet flowing through the runner is known, it becomes possible to determine the frictional losses in a Bánki turbine runner and the hydraulic efficiency of the runner, too.

REFERENCES

[1]   Czibere Tibor (2009). Az el nem évülő Bánki-turbina létrehozója 150 éve született. *GÉP*, 60. évf., 3. sz., pp 9–15.

[2]   Varga, J. (1959). Tests with the Banki water turbine. *Acta Technica Academicae Hungaricae*, 27 (1/2), pp. 79–102.

[3]   Mockmore, C. A. – Merryfield, F. (1949). *The Banki Water Turbine*. Engineering Station Bulletin Series, No. 25, Oregon State College, Corvallis, Oregon, USA.

[4]   Bánki Donát (1920). *Energiaátalakulások folyadékokban*. 2. kiadás, Budapest, Franklin.

POTENTIAL FUTURE FOR SRM AND SYNCRM IN AUTOMOTIVE APPLICATIONS

PÉTER ISTVÁN HORVÁTH, KÁROLY JÁLICS

University of Miskolc, István Sályi Doctoral School of Mechanical Engineering Sciences,
3515 Miskolc-Egyetemváros,
peterhorvath@hotmail.de, machijk@uni-miskolc.hu
https://orcid.org/0000-0003-0749-7569 (Jálics K.)

Abstract: The global warming is affecting the life of all of us. Several sectors are contributing to the greenhouse emission. One of the larger contributors is the transportation, in which the road transport accounts for the CO_2 emission with a significant percentage. In order to reduce the CO_2 emission vehicles are becoming hybridized, electrified. Currently in the electrical vehicles the Permanent Magnet Synchronous Machines (PMSM) outweigh other types of electric motors. The application of the electric machines with rear-earth material is becoming more and more difficult, and costly. Also, the technological improvements of other types of electric machines make them potential candidates to replace the PMSM. As a potential alternative the Switched Reluctance (SRM) and the Synchronous Reluctance Machines (SyncRM) can be considered. The application of such electric machines without permanent magnet would further contribute to the reduction of the greenhouse emissions considering the well-to-wheel cycle. The goal of the following review is to summarize the sectors that have major impact on the CO_2 emission, summarize the current trends followed in order to reduce the CO_2 emission in the road transport sector, review why the currently preferred PMSM electric motors might have limitations in automotive applications in the future, and review why and how the SRM and SyncRM could be alternative solutions for the PMSM, which is finally summarized in a datum method based comparative evaluation.

Keywords: *environmental pollution, electric vehicles, electric motors, Switched Reluctance Machine (SRM), Synchronous Reluctance Machine (SyncRM)*

1. INTRODUCTION

As a result of the environmental pollution global warming poses a huge challenge for the entire world. The deteriorating atmospheric condition along with the global warming mainly caused by the high CO_2 emissions has triggered international initiatives to reduce the global CO_2 emission. The new directives and regulations set strict targets for the emission level itself, and also define certain dates when the regulations go into effect. The road transport has a major portion in the energy consumption, and through that in the CO_2 emission. Based on statistical data transport contributes to more than 30% to the final energy consumption (https://ec.europa.eu/eurostat/web/main/data/database).
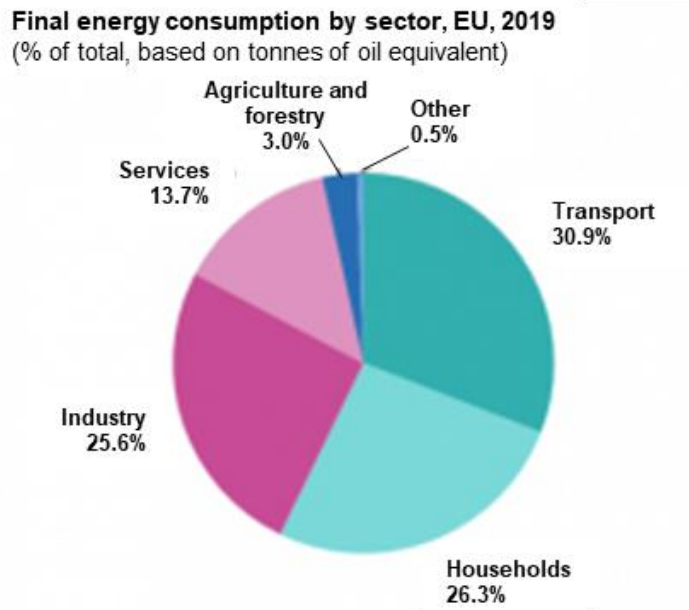
Final energy consumption by sector, EU, 2019
(% of total, based on tonnes of oil equivalent)

Figure 1
Final energy consumption by sector in the EU

According to the statistics of the European Environment Agency road transport accounts for more than 70% of the total greenhouse gas emission caused by the transport sector (https://ec.europa.eu/eurostat/web/main/data/database).
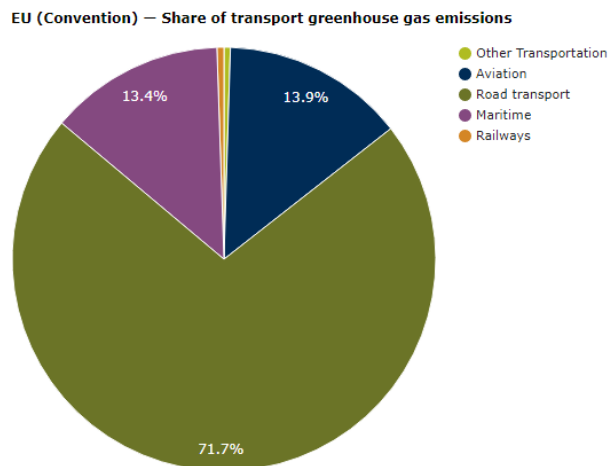

Figure 2
Share of transport greenhouse gas emission in the EU

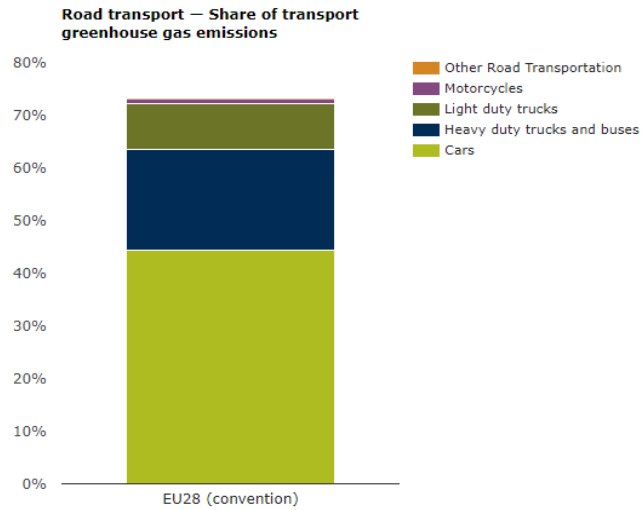Further breaking down the road transport greenhouse gas emission it becomes visible that more than half of the road transport emission is caused by the cars (https://ec. europa.eu/eurostat/web/main/data/database).

Road transport — Share of transport greenhouse gas emissions

Legend:
- Other Road Transportation
- Motorcycles
- Light duty trucks
- Heavy duty trucks and buses
- Cars

Figure 3
Road transport share in the EU

The electrification of the cars offers a huge potential to reduce the CO_2 emission. The required sharp decrease on CO_2 emission of new vehicles on fleet level forces the car manufacturers to increase the volume of the electrified vehicles in their fleet. In addition, governmental incentives are also fuelling the purchase of electric vehicles (https://ec.europa.eu/eurostat/web/main/data/database).
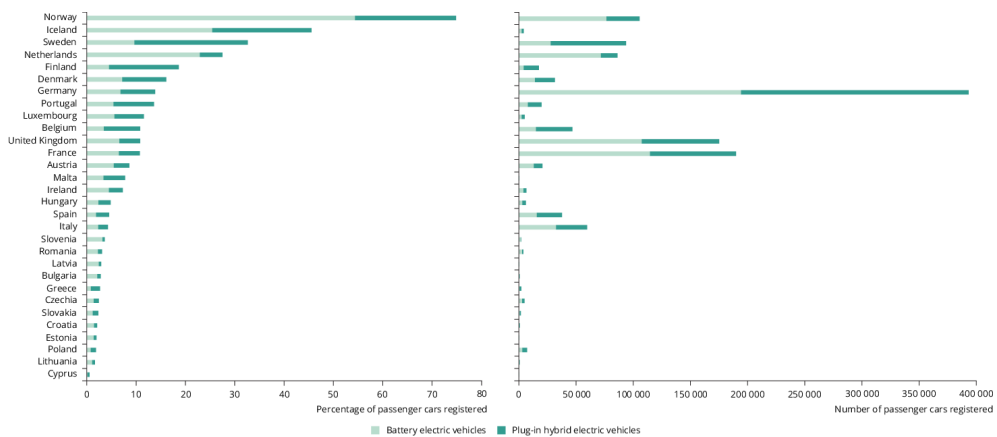

Figure 4
Newly registered electric cars in EU27, Iceland, Norway and UK in 2020

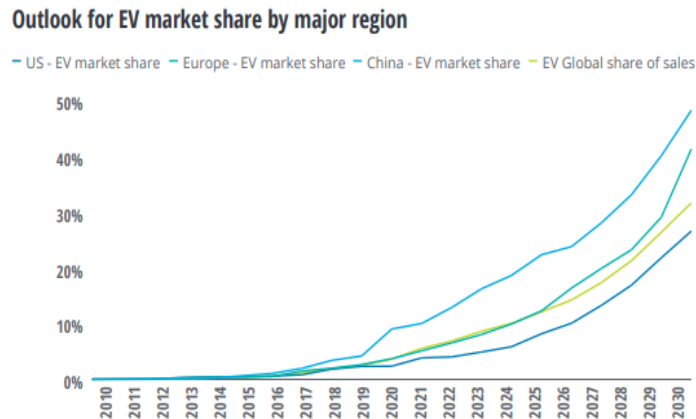Electric vehicle sales forecast shows a rapid growth in the upcoming decade [1].

Outlook for EV market share by major region

— US - EV market share   — Europe - EV market share   — China - EV market share   — EV Global share of sales

Figure 5
Outlook for EV market share by major region [1]

2. OVERVIEW OF ELECTRIC VEHICLES HEV, PHEV, BEV, FUEL CELL

The electrification of the cars can be achieved in multiple ways. Hybrid electric vehicles (HEV) combine the Internal Combustion Engine (ICE) with Electric Machines (EM). They offer fuel consumption advantages compared to the pure internal combustion engine vehicles. This results from the ability to downsize the engine and to operate it nearer to optimal conditions and, in some driving conditions, the ability to recover kinetic energy during braking [2]. Literature and studies show that downsizing the internal combustion engine, shifting the operating point and combining with regenerative braking can result in significant fuel consumption reduction. According to different literatures, the reduction can be up to 45%.

A step forward in the vehicle electrification is the Plug-in Hybrid Electric Vehicle (PHEV). This type of electric vehicle has also an ICE and an electric motor. However contrary to the HEV, where the electric motor is mainly used for boost, the PHEV offers a shorter range of electric driving. Depending on the design the electric driving distance can be up to 50 km. In the PHEV charging is not just by regenerative braking, but also possible by external electric sources via a charging port. Due to the electric driving capability PHEVs have a larger battery than the HEVs. In comparison to the HEV, PHEV offers 10% fuel consumption reduction additionally.

Contrary to HEV and PHEV, which are partially electric vehicles, Battery Electric Vehicles (BEV) are fully electric vehicles. BEVs don't have a secondary source of propulsion. The electrical energy used by the electric machine of the BEV is stored in battery packs. Due to the technology improvement in the past years, which resulted in efficiency increase of the overall drivetrain, and improved battery design, and depending on the battery size the electric range of the electric vehicles can reach over

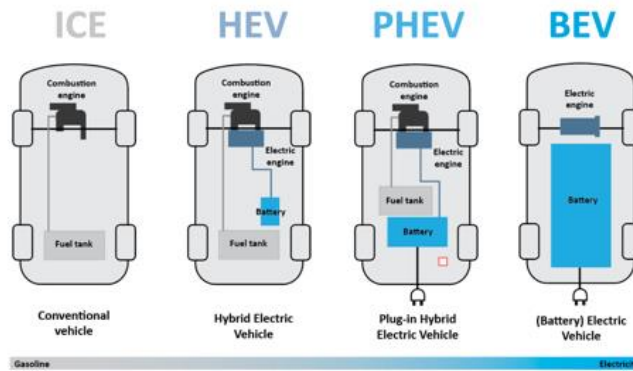400-500 km. A high-level topological comparison between the ICE, HEV, PHEV and BEV can be seen in *Figure 6* (https://europe.midtronics.com).

Figure 6
Topological comparison between ICE, HEV, PHEV and BEV vehicles

3. ELECTRIC MOTORS IN DIFFERENT ELECTRIC VEHICLES, E-DRIVES

Regardless whether partial or full electric vehicle, they are common in the usage of at least one electric machine. In the hybrid and full electric vehicles not all types of electric machines used. The electric machines used in the hybrid and electric vehicles must fulfil certain performance and commercial requirements. They must have high efficiency, high starting and rated torque, overload capacity, high reliability, high power density and specific power, wide operating speed range, and of course all this at a feasible cost. Based on today's electric motor technology the induction and synchronous electric machines can fulfil these requirements.
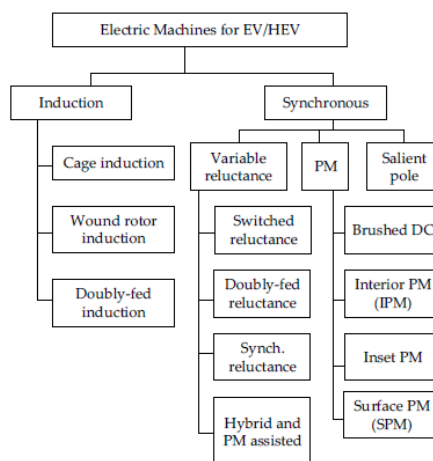

Figure 7. *Motor types available for hybrid electric/electric vehicles* [3]

In the hybrid and electric vehicles, the application of the induction machines (IM) and the permanent magnet synchronous machines (PMSM) outweigh the application of other machines. The following table provides a high-level overview on the application of electric machines in different electric vehicle makes.

Model	Year	Motor Type	Peak Power [kWp]	Peak Torque [Nm]	Max Speed [rpm]	Poles	Peak Specific Power [kW/kg]	Peak Power Density [kW/L]
Roadster	2008	IM	215	370	14800	4	4,05	−
Tesla S60	2013	IM	225	430	14800	4	−	−
Model 3	2017	PM	192	410	18000	6	−	−
Prius	2004	PM	50	400	6000	8	1,1	3
Prius	2010	PM	60	207	13500	8	1,6	4,8
Prius	2017	PM	53	163	17000	8	1,7	3,35
Accord	2006	PM	12	136	6000	16	0,53	2,83
Accord	2014	PM	124	-	14000	8	2,9	2,93
Spark	2014	PM	105	540	4500	12	−	−
Volt	2016	PM	111	370	12000	12	−	−
Bolt	2017	PM	150	360	8810	8	−	−
Leaf	2012	PM	80	280	10390	8	1,4	4,2
Leaf	2017	PM	80	280	10390	8	1,4	4,2
Camry	2007	PM	70	270	14000	8	1,7	5,9
Camry	2013	PM	70	270	14000	8	1,7	5,9
Lexus	2008	PM	110	300	10230	8	2,5	6,6
Sonata	2011	PM	30	205	6000	16	1,1	3
BMW i3	2016	PM	125	250	11400	12	3	9,1

Figure 8
Motor types used in electric vehicles and their specification [3]

As it can be seen the permanent magnet synchronous machine has been the preferred solution. The reason is that the PMSM machines have a very high torque density, high efficiency, however in order to have these advantages a permanent magnet has to be in places either on the surface of the rotor, or integrated inside the rotor. In order to have high torque/power density, high efficiency, and also be resistant to demagnetization during field weakening high-energy rare-earth magnets are used in permanent magnet machines.

4. PERMANENT MAGNET COST, UNEVEN DISTRIBUTION OF RARE-EARTH MATERIAL PRODUCTION, SUPPLY

The permanent magnets have high cost, and they take up a significant portion of the total cost of a permanent magnet machine, even though they represent a small portion of the total weight of the motor [4]. Depending on the application the rare-earth permanent magnets can take even more than 50% of the total cost of the electric machine.

The rare-earth magnet supply chain can be divided into five stages: (a) mining, milling and concentration of the ore, (b) separation into individual rare-earth oxides, (c) rare-earth metal production, (d) alloy or powder production, and € magnet

manufacturing [5]. Out of the five stages the production is concentrated among few countries, which tends to result in a monopolistic situation, seriously affecting other industries. China dominates the rare-earth production, even though they hold only about half of the known world reserves [6]. As it can be seen in *Figure 9*, China holds 84% of the world production [4].
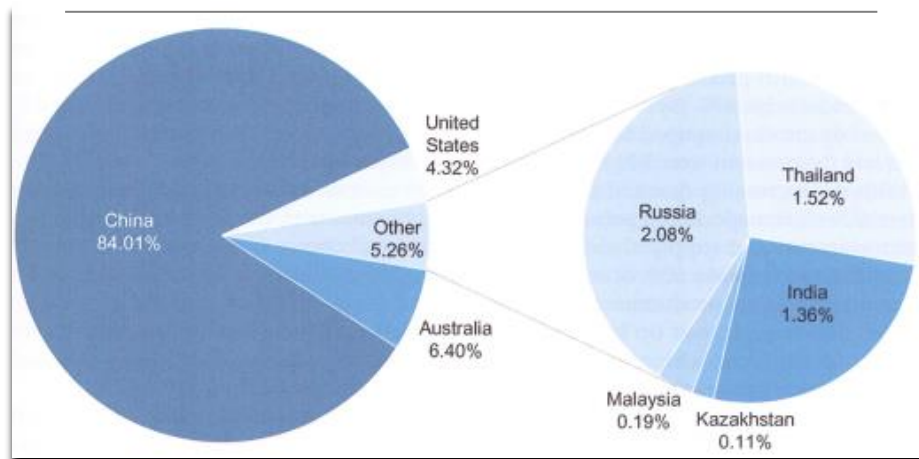

Figure 9.
World mine production of rare-earth materials by country [4]

As China is the largest producer of the rear-earth materials, they have a significant control over the availability and the price of the material. Through export quota regulations the market would further be distorted.

In addition to the higher cost and uneven distribution of the rare-earth material production, in the past time serious supply issues happened with the rare-earth materials due to shortages in the production. Rare-earth materials are not just used more and more in the automotive industry, but it is also used in application of other industries, like PC, cell phones, batteries etc. Due to the increase in the demand in all the industries, on one hand the shortage further increased the price, on the other hand it slowed down or stopped completely vehicle production lines.
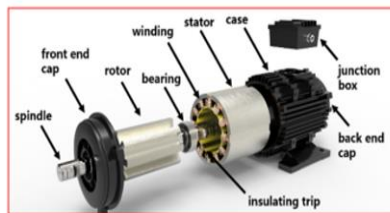
Because of these serious issues, disadvantages an alternative electric machine solution should be applied in the hybrid and electric vehicles in order not to be exposed to price volatility, supply chain issues and shortages. In order to mitigate the risk, the alternative solution could be another synchronous machine, the switched and synchronous reluctance machines.

5. APPLICATION OF SRM AND SYNCRM

The Switched Reluctance Machine offers a low cost, robust and simple construction, combined with reliable operation, which is suitable for usage in high speed and high temperature applications. Its simple design includes a stator made of stamped silicon

steel with salient, inward projected poles. Depending on application the stator can have different number of poles, but most of the motors on the market have 6 or 8 stator poles. The stators also carry coils, which on the opposite poles are connected in series. The rotor has a similar salient, but outward projected pole design, they do not carry coils, and opposite to a PMSM they do not have any permanent magnets. The shaft of the SRM is a simple turned steel, while the winding is of copper. *Figure 10* compares the construction of the SRM to the PMSM, visualizing the main differences.
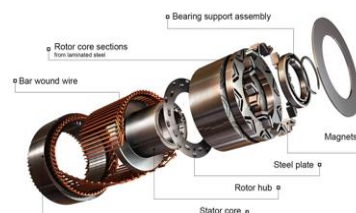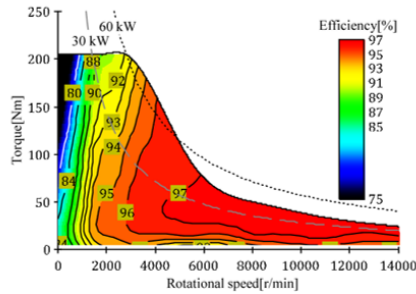

Figure 10
Comparison of the SRM and PMSM construction [7, 8]

The lack of permanent magnet (rare-earth material), simpler, less complicated design, simple manufacturing offer significant advantages in terms of cost, independency from rare-earth material, and supply chain security.

Additional advantages of an SRM over a PMSM are the simple rotor design, which due to the lack of magnets, windings offer higher achievable operating speed, better acceleration. Because of the lack of rear-earth magnet, the machine can withstand higher operating temperature, which allows a less sophisticated, simpler cooling design in the automotive applications. In the automotive applications additional significant advantages of an SRM are the potential usage in harsh environment, and the so-called limp home capability. In case of fault in any of the windings in an SRM application the SRM can still work at reduced load, allowing the vehicle still to limp to the nearest service station. The SRM has high efficiency over a wide speed and load range, however it can be seen that the higher efficiency is available from the mid-range speed. A comparison of the efficiency maps between an SRM and PMSM are shown in *Figure 11*.
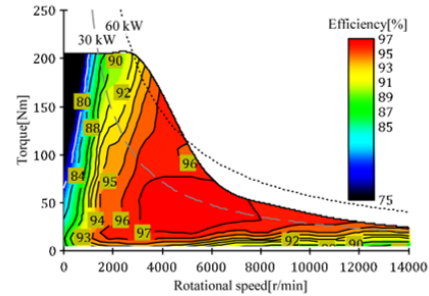
• Efficiency map of SRM

• Efficiency map of PMSM

Figure 11

Efficiency map comparison of SRM and PMSM [9]

It is visible, that at low speed, below 2,000 rpm the PMSM offers a slightly better efficiency, however between 2,000–5,000 rpm the SRM efficiency matches that of the PMSM, and above 5,000 rpm the SRM is clearly provides better efficiency.

Disadvantages of an SRM are the higher torque ripple and higher acoustic noise. *Figure 12* provides a high- level summary on noise and vibration sources for electric motors.
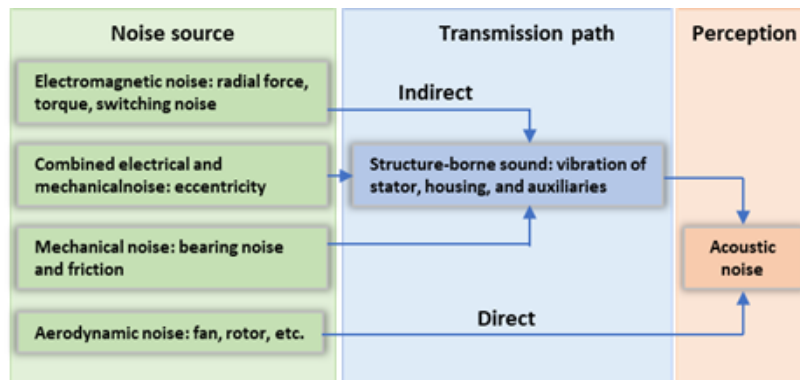
Figure 12

Noise and vibration sources for electric motors [4]

Due to the salient pole construction of SRMs, when a phase is excited with current, the flux penetrates into the rotor, mostly in the radial direction, and generates radial forces [4]. The radial forces deform the stator core, which results in airborne borne noise. This airborne noise can become audible around the electric motor directly. The acoustic noise can be optimized by active (i.e. additional ribbing on the stator) and passive (i.e. encapsulation of the SRM) countermeasures, reducing the impact of this disadvantage on the overall evaluation.

A very similar construction to the SRM is the Synchronous Reluctance Machine (SyncRM), however in case of the SyncRM the stator does not have salient poles, and the rotor has either a radially or axially laminated core. Keeping important advantages of the SRM, like low cost, simple design, application in high speed and high temperature environment, the SyncRM offers additional advantages in terms of less torque ripple, less acoustic noise, higher efficiency, simpler inductance waveform, and less expensive power electronics as the SyncRM requires lower phase currents. Comparing the different propulsion types for hybrid and electric vehicle applications, one can summarize the characteristics showing importance in automotive applications. One potential approach, which is based on the datum method is shown in *Table 1*.

Table 1
Comparative evaluation of PMSM, SRM and SyncRM
for automotive applications

Propulsion type	PMSM	SRM	SyncRM
Characteristics			
Power density	5	3,5	3
Efficiency	5	3,5	4
Controllability	4	3	3,5
Design complexity	3	4	4
Speed range	3,5	4	4
Temperature resistance	3,5	4	4
Supply chain security	3	5	5
Reliability	4	5	5
NVH	4	3	3,5
Cost	3	4	4,5
Total:	**38**	**39**	**40,5**

In the datum method the evaluation criteria are listed vertically, which are the characteristics in this particular case. The PMSM has been selected as the datum, and the SRM and respectively the SyncRM have been selected as the potential alternative solutions. Instead of the general "+"/"–", numerical (1–5) evaluation has been used, where "1" is the worst, and "5" is the best. Considering the subjective evaluation results, it is visible that the SRM and SyncRM can be competitive with PM which is dominantly used in today's hybrid and electric vehicle applications, and depending on the development preferences the advantages of an SRM and SyncRM could even be a better option for the automotive applications.

6. CONCLUSION

Researches have recently been focusing already on the SRM and SyncRM. Further study, analysis and development of SRM and SyncRM for automotive applications seems to be reasonable, as depending on the preferred characteristics the SRM and especially the SyncRM can indeed be considered as a potential candidate to replace the PMSM. Some characteristics of SRM and SyncRM are comparable, some characteristics of the SRM and SyncRM are even better than the PMSM characteristics. In addition to the cost and supply chain security, reduction of dependency on limited the number of rear-earth material producers are all pushing for alternative EM solutions. Simple design and manufacturing of the SRM and SyncRM are also important aspects. Disadvantages like higher torque ripple and higher acoustic noise can be improved with active and passive countermeasures. Additional advantage of the SRM and SyncRM that they can still work at reduced load in case of fault in any of the windings, which allows vehicle to reach the nearest service station in a limp-home mode.

REFERENCES

[1] Hamilton, J. – Walton, B. – Ringrow, J. – Alberts, G. – Fullerton-Smith, S. – Day, E.: Deloitte Insights, Electric Vehicles, Setting a course for 2030, analysis, HIS Market, *EV-Volumes.com*, Deloitte University EMEA CVBA, p. 7

[2] Othaganont, P. – Assadian, F. – Auger, D. J. (2016). Multi-objective optimisation for battery electric vehicle powertrain topologies, *Journal of Automobile Engineering*, Institution of Mechanical Engineers, 23 August 2016, p. 1, https://doi.org/10.1177/0954407016671275.

[3] Agamloh, E. – von Jouanne, A. – Yokochi, A. (2020). *An Overview of Electric Machine Trends in Modern Electric Vehicles*. 17 April 2020, pp. 3–4. https://doi.org/10.3390/machines8020020.

[4] Bilgin, B. – Weisheng, J. – Emadi, J. A. (2019). *Switched Reluctance Motor Drives, Fundamentals to applications*. CRC Press, ISBN: 978-1-138-30458-8, pp. 20–21, p. 580, p. 578.

[5] *U.S. Department of Energy, Critical Materials Strategy*. December 2011. http://energy.gov

[6] Parthemore, C. (2011). *Elements of Security: Mitigating the Risk of U.S. Dependence on Critical Minerals*. Washington DC: Center for a New American Security.

[7] Ling, X. – Li, T. – Liu, Q. (2019). A Multi-Physics Modelling-Based Vibration Prediction Method for Switched Reluctance Motors. *Applied Sciences*, 9, 4544; p. 3, https://doi.org/10.3390/app9214544.

[8]   Omekanda, A. M. (2013). Switches reluctance machines for EV and HEV propulsion: State-of-the-art. *Electrical MachinesDesign Control and Diagnosis (WEMDCD), IEEE Workshop on*, pp. 70–74. https://doi.org/10.1109/WEMDCD.2013.6525166.

[9]   Kiyota, K. – Sugimoto, H. – Chiba, A. (2012). Comparison of energy consumption of SRM and IPMSM in automotive driving schedules. *IEEE Energy Conversion Congress and Exposition (ECCE)*, Figure 2 from Comparison of energy consumption of SRM and IPMSM in automotive driving schedules | Semantic Scholar, Figure 3 from Comparison of energy consumption of SRM and IPMSM in automotive driving schedules | Semantic Scholar, https://doi.org/10.1109/ECCE.2012.6342729.

3D PRINTED PLANETARY GEARBOX FOR ROBOTIC ARM JOINTS

FILIP HRDLIČKA

University of West Bohemia, Department of Machine Design
Univerzitní 22, 301 00 Plzeň
ficeriov@kks.zcu.cz
https://orcid.org/0000-0003-2815-0062

Abstract: 3D printing technology has become very popular in last several years as a cheap way how to make different parts. 3D printing is as a perfect tool for prototyping of various, mostly difficult, structures which is the reason why it is more and more use in mechanical design. This article is focused on assessment if 3D printing technology can be used for creating light, durable and cheap variation of classic metal or moulded plastic gearboxes for electric motors which can be used for low cost robotic arms. For this purpose was in CAD software designed a small two-stage planetary gearbox with identical stages. All parts of gearbox were printed by FDM 3D printer with most common printing material PLA. The gearbox has been tested on noise, durability, resistance and maximum load on lever to find out where can be potential of 3D printed gearboxes.

Keywords: 3D printing, Gearbox, Robotic arm, Stepper motor

1. INTRODUCTION

Robotic arms nowadays mostly using electric motors for propulsion of each their joint. Every electric motor need to be connected with joints of a robotic arm by some kind of propulsion which transfer revolutions and torque, because revolutions of the electric motors are high and torque low. These propulsions can be divided into two categories, distant propulsion and direct propulsion.

Distant propulsion means that the motor is placed before the joint which is propelled. For transmission and transfer torque and revolutions are mostly used timing belts. Mostly is the motor close to the previous joint what helps decrease load of previous motor thus increase maximum manipulating weight of the robotic arm. Next advantages of this solution are low weight and low number of parts. Disadvantages of this solution are requirements to belt tensioning and more frequent maintenance.

Direct propulsion, as the name suggests, means that the motor is placed directly in the joint which is propelled and for transfer torque and revolutions are used different kinds of gearboxes. Gearboxes which are mostly used are planetary gearboxes, harmonic gearboxes, cycloidal gearboxes, gearboxes with worm gears or gearboxes with spur gears. Advantages of gearboxes are small dimensions and

closed system so they do not need so frequent maintenance. Disadvantage of direct propulsions is high weight placed on the joint what means that the more far from center of gravity of the robotic arm is this propulsion placed, the more maximum manipulating weigh of the robotic arm is decreasing. Another disadvantage is high price of these gearboxes in comparison with timing belts.

This article deals with design, production, tests and comparison of a prototype 3D printed planetary gearbox as a potential alternative to metal gearboxes for small robotic arms.

2. DESIGN OF THE PLANETARY GEARBOX

As a final design was chosen a planetary gearbox concept which combine properties of compact dimensions and simple way to print [1]. For initial design of composition was used online software Planetary Gear Simulator [2] which is fast and easy tool for calculation of number of gears, number of their teeth and transmitting ratio of planetary gearbox. The gearbox is designed as two-stage with similar revolutions transfer ratio 5 : 1 per to stage. Total ratio of the gearbox is 25 : 1 for revolutions. Every stage of the gearbox has 1 sun gear, 3 planet gears and 1 ring gear. The sun gears are input periphery and the planetary gears attached in carriers are output periphery. The ring gears are rigid. All gears are made with a double-helical gearing. The double-helical gearing was chosen due to its useful ability self-centering – do not produce axial forces on the gearbox. This gearbox was designed for stepper motor NEMA 17HS4401 [3].

Whole gearbox was designed in the CAD software Autodesk Inventor 2019 which contains gears design utility. This utility can generate external or internal spur or helical gears with involute gearing. Input values are a module, axis distance, number of teeth, width of gears and angle of teeth. To get the gears for the planetary gearbox is necessary to generate two gear pairs with helical gearing, one with external gears and second one with internal and external gear *(Figure 1)*. These gears are mirrored around the lateral plane which creates double-helical gearing. Final dimensions of the gears are listed in the *Table 1*.

Table 1
Final dimensions of gears

		Sun gears	Planetary gears	Ring gears
Number of teeth	z [–]	15	22	60
Module	m [mm]	0.75	0.75	0.75
Tip circle	d_a [mm]	13.219	18.655	45.475
Pith circle	d [mm]	11.647	17.082	46.587
Root circle	d_f [mm]	10.020	15.456	48.7
Module correction	[–]	0.1656	0.1656	0.1582
Width	t [mm]	10	10	5

As shown in *Table 1*, the ring gears have only a half width as other gears, this difference has a reason. All gears have double-helical gearing and that means that during assembling they cannot be simply inserted. From this reason are the ring gears divided into half so they can be slid on the planetary gears from sides.
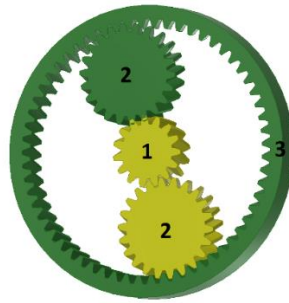

Figure 1. *The yellow pair represent the sun gear (1) and the planetary gear (2), the green pair represent the planetary (2) and the ring gear (3)*
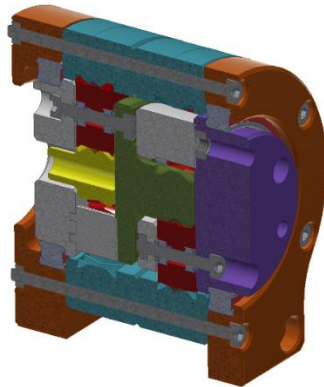

Figure 2. *Cut through the final model of the planetary gearbox*
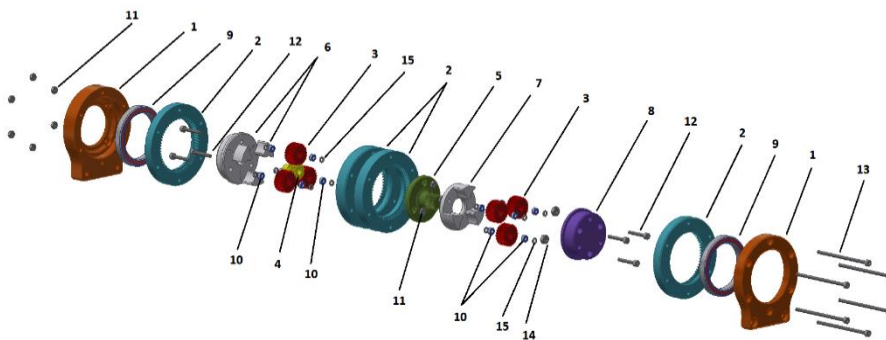

Figure 3. *Exploded view of the designed planetary gearbox*

The final model of gearbox *(Figure 2, Figure 3)* is assembled from parts: 1 – 2× covers with housing for bearings (9), 2 – 4× ring gears, 3 – 6× planet gears, 4–1× sun gear of first stage, 5 – 1× sun gear of second stage as a second part of carrier of first stage, 6 – 1× first part of carrier of first stage, 7 – 1× first part of carrier of second stage, 8 – 1× second part of carrier of second stage/output flange, 9 – 2× bearings 6808-2RS (40 × 52 × 8), 10 – 12× bearings MR63-2Z (3 × 6 × 2.5), 11 – 12× hex nuts M3 (DIN 934), 12 – 6× Hex socket bolts M3 × 20 (DIN 912), 13 – 6× hex socket bolts M3 × 60 (DIN 912), 14 – 3× hex nuts M4 (DIN 934), 15 – 12× 3D printed spacer rings (3.3 × 5 × 1).

Part no. 4 (sun gear) is input peripherals connected directly to chamfered shaft of the stepper motor. Part no. 8 (flange) is output peripherals with connection dimensions M4 3 × 120° on pitch circle 30 mm.

3. PRODUCTION OF THE PROTOTYPE

Production of gearbox consists from 3D printing of parts (gears, covers, etc.) and their assembly with bought parts (bearings, bolts, etc.).

3.1. 3D printing

For 3D print was used FDM 3D printer Artillery sidewinder X1, as printing material was used the most common material – PLA. All parts were exported into STL format and prepare for print in PrusaSlicer. Axis of all parts were oriented vertical to the pad of the 3D printer *(Figure 4)*. Before export into STL were all parts adjusted to tolerance of 3D printing. Tolerance of 3D printed parts is approximately –0.2 mm. Holes for bolts got +0.3 mm tolerance for guaranteed clearance, holes for nuts got +0.15 mm for overlap fit and holes for bearings got +0.1 mm for overlap fit.

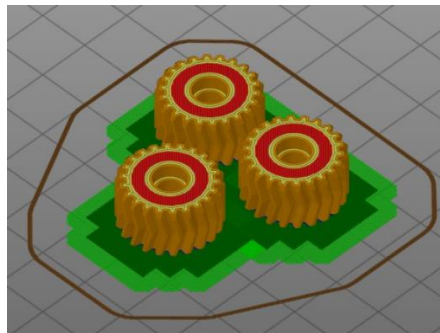***Figure 4.*** *The planetary gears prepared for print in PrusaSlicer*

Parameters of printing were focused to the best precision and details of printed parts. [4] The sun and the planetary gears were printed by 0.1 mm thick layer, 30% gyroid infill and with 2 layer thick raft which ensured accurate width of gears. The ring gears and all other parts were printed by 0.2 mm thick layer with 30% grid infill and

without raft. Speeds of the 3D printer were 60 mm/s for perimeters, 15 mm/s for small perimeters, 30 mm/s for outside perimeters, 80 mm/s for infill, 30 mm/s for full fill, 20 mm/s for infill of thin walls, 20 mm/s for top 3 layers, 25 mm/s for first layer, 50 mm/s for bridges and 130 mm/s for rapid traverse.

3.2. Assembling the gearbox

Printed parts were assembled with bearings, nuts and bolts *(Figure 5)*. The final gearbox is 65.5 mm long, 78 mm high and 70 mm wide where 70 mm is outside diameter of the ring gears. Total weight is 249 g where 169.34 g represent printed parts. Total cost of the gearbox are 195.73 Kč – 7.67 EUR (exchange rate from 24. 11. 2021) where 67.56 Kč – 2.65 EUR represent cost spent on printing material. After assembly was measured backlash of the gearbox which is 0.57° (34').
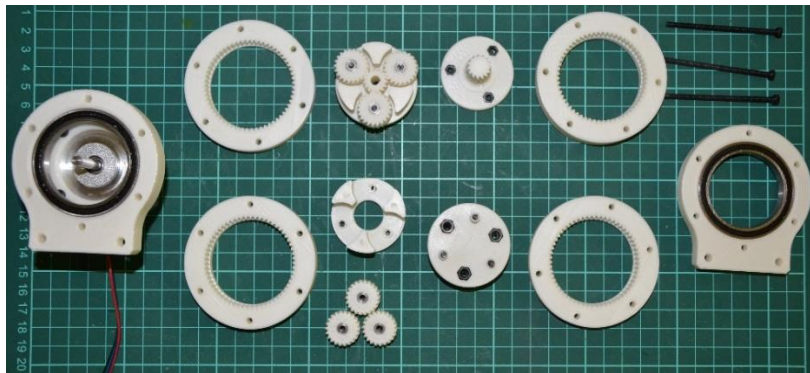

Figure 5. *Printed parts of the gearbox assembled with bearings and nuts*

4. TESTING OF THE GEARBOX

Tests were focused on four categories, noise, resistance, maximum load capacity and durability.

Noise was compared with noise of used stepper motor which was mentioned. At constant speed was measuring noise of the stepper motor without the gearbox, the motor with the gearbox without grease and the motor with the gearbox with grease. All these three measurements of sound pressure level were long one minute and made at a constant distance of 10 cm. From data was compute average level of noise. The first case had noise 48 dB(A). In the second case was measured average noise 63 dB(A) and the last case had average noise 59 dB(A).

Second test was focused on resistance of the gearbox. Subject of test was measuring temperature of the stepper motor and compare how much resistance of the gearbox affects it. Test compare three cases, motor without load (motor only), motor with the gearbox without grease and motor with the gearbox with grease. Temperature was measured for 6 hours in 10min. intervals for first hour. Between first and second hour in 15min. intervals and from second to sixth hour in 1 hour intervals.
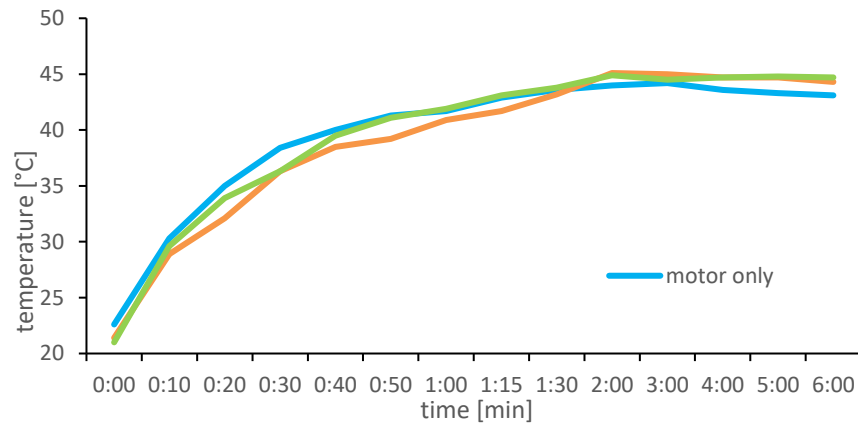
Figure 6. *Temperature of the motor in time*

As shown in *Figure 6*, temperature in all three cases raised up from room temperature (on average 21.5 °C) very quickly in first several minutes. After 2 hours of continuous run the temperature has stabilized between 44–45 °C. In the first case temperature after third hour started slightly decline to the final temperature 43.1 °C. It could be caused by changes temperature in the room during day. This test find out that resistance of the gearbox do not have any significant effects on connected motor. Third test was focused to find maximum load torque which is the planetary gearbox able to transfer. On the 3D printer was printed testing arm with hole distant 200 mm from the axis of the gearbox. In the hole was hooked up a bucket with load which was increased till the gearbox failed.

Figure 7. *Failed testing arm*

Figure 8. *Failed part of the gearbox – output flange*

Achieved load when the gearbox failed was 13.2 kg what represent torque moment 25.9 Nm. First symptoms, visible deformation and crackling sound, appears at 12.3 kg what represent torque moment 23.54 Nm. As shown in *Figure 7* and *Figure 8*, parts which were damaged during the test were testing arm and output flange of the gearbox. On output flange is obvious how torque twisted holes with bolts and also crack in place where is placed bearing. This happened due to sparse infill of this component. If the infill would be denser, would be this component able to transfer even bigger load.

Last test was focused on durability. During all tests input sun gear did over 300,000 revolutions, then was the gearbox disassembled and the sun gear checked how much was abraded. As shown in *Figure 9*, the sun gear has no visible symptoms of abrasion or damage.

Figure 9. *The input sun gear after more than 300,000 revolutions*

5. COMPARISON

On the market we can find several types of gearboxes for stepper motors. To compare this 3D printed gearbox were chosen gearboxes with similar parameters – planetary layout, output torque and suitability for stepper motor NEMA 17HS4401. These parameters meets metal gearbox GP42-S2-21-SR from company Nanotec [5] and metal gearbox PLE17-G20 from company Stepperonline [6].

Table 2

Comparison of gearboxes

		GP42-S2-21-SR gearbox	PLE17-G20 gearbox	3D printed gearbox
Reduction ratio	[1]	20.64 : 1	20 : 1	25 : 1
Max. output torque	[Nm]	17.7	12	<23.54
Dimensions (W × H × L)	[mm]	42 × 42 × 50.9	42 × 42 × 67	70 × 78 × 65.5
Weight	[g]	380	382	249
Max. backlash	[°]	51	19	34
IP protection	[–]	IP54	IP54	–
Service life	[h]	10,000	20,000	–
Noise	[dB(A)]	–	<55	59
Price	[EUR]	109.3	46.49	7.67

Although 3D printed gearbox is bigger, do not have IP protection and we do not know its service life, *Table 2* shows, that for its small weight and especially low price, it can be good solution for undemanding applications like small robotic arms.

6. CONCLUSION

The goal of this article was create functional 3D printed planetary gearbox as cheap alternative to existing manufactured gearboxes for low cost robotic arms. Tests have shown that is possible with most common 3D print technology and printing material create light, cheap and durable gearbox which has potential works long time and with medium size torque. In any case there is still a lot of space how to improve the gearbox and reach better parameters. Big potential is both in the design and in the material where can be used material with better mechanical parameters as polypropylene or nylon. Can be also used another and still cheap 3D printing technology as SLA which has better resolution than FDM what can reduce size of whole gearbox.

REFERENCES

[1] García, P. L. – Crispel, S. – Saerens, E. – Verstraten, T. – Lefeber, D. (2020). Compact Gearboxes for Modern Robotics: A Review. *Frontiers in Robotics and AI*, Vol. 7, Article 103, August 2020. https://doi.org/10.3389/frobt.2020.001

[2] *Planetary Gear Simulator*. http://www.thecatalystis.com/gears/ (2021/12/13).

[3] *NEMA 17HS4401 datasheet*. http://www.datasheetcafe.com/17hs4401-data sheet-stepper-motor/ (2021/12/13).

[4] Kumar, K. M. – Pandey, P. M. – Wimpenny, D. I. (2019). *3D Printing and Additive Manufacturing Technologies*. ISBN 978-981-13-0304-3, Springer Nature, Singapore, https://doi.org/10.1007/978-981-13-0305-0.

[5]   *Nanotec*. https://en.nanotec.com/products/2802-gp42-s2-21-sr/ (2021/12/13).

[6]   *Stepperonline*. https://www.omc-stepperonline.com/ple-series-planetary-gear box/ple-series-planetary-gearbox-gear-ratio-20-1-backlash-20-arc-min-for-nema-17-stepper-motor.html?mfp=287-gear-ratio%5B20%5D/ (2021/12/13).

THE EFFECTS OF WATER-CUO NANOFLUID FLOW
ON HEAT TRANSFER INSIDE A HEATED 2D CHANNEL

MOHSEN KHALILI NAJAFABADI[1] – GABRIELLA BOGNÁR[1, *] –
KRISZTIÁN HRICZÓ[2]

[1]*University of Miskolc, Department of Machine and Product Design,*
3515 Miskolc-Egyetemváros,
femohsen@uni-miskolc.hu
[2]*University of Miskolc, Institute of Mathematics,*
3515 Miskolc-Egyetemváros,
mathk@uni-miskolc.hu
[*]*Correspondence: v.bognar.gabriella@uni-miskolc.hu*
https://orcid.org/0000-0002-4070-1376 (Bognár G.)
https://orcid.org/0000-0003-3136-4248 (Hriczó K.)

Abstract: The velocity distribution and heat transfer improvement in a two-dimensional channel filled with a water-CuO nanofluid is numerically studied. The nanofluid flow is assumed laminar and one-phase with Newtonian behaviour. Pure water is considered as the base fluid, and water-CuO nanofluid with four different volume fractions of CuO nanoparticles are examined. A constant heat source–sink is considered to cover the entire length of the bottom wall of the channel while the upper wall is assumed thermally insulated. The control volume technique is used to discretize the governing differential equations, and the SIMPLE algorithm is used to solve the velocity-pressure coupling. A CFD simulation is applied on nanofluid flow utilizing ANSYS FLUENT to solve the governing equations of the flow. The effects of nanoparticle volume fraction on the heat transfer, velocity profile, wall shear stress, skin friction coefficient, and Nusselt number along the channel have also been examined. The results confirm that the volume fraction of nanoparticles plays an important role in heat transfer enhancement and hydrodynamic behaviour of flow. The results are presented in figures and tables.

Keywords: Nanofluid, CFD, heat transfer enhancement, numerical method, channel, 2D

1. INTRODUCTION

Conventional fluids have restricted heat transfer potential due to their poor thermophysical properties such as thermal conductivity. Therefore, scientists have attempted to resolve these kinds of difficulties by enhancing the thermal properties of these fluids to achieve more advanced capabilities. The number of industrial demands that might benefit from improved heat transfer fluids is infinite, including applications in hot rolling, paper drying, biomedicine, food processing, nuclear reactors, and so on. As a result, several strategies have been used to improve the thermal properties of conventional fluids.

Dispersion of nanoparticles in a base fluid was one of the first approaches. In fact, thermal characteristics can be improved by adding particles of different materials with a better thermal conductivity than the base fluid [1]. For example, metal particles have a greater thermal conductivity than the base fluid in general. Stephen [2] was the first to develop this approach, which he invented the word nanofluid in enhancing thermal conductivity. Because of the extremely high specific surface area of nanoparticles, nanofluids have a significantly greater effective thermal conductivity, making them a promising candidate for heat transfer applications. This method of improving thermal properties has received a lot of attention in a variety of other applications and academia. The study of the thermal physical characteristics of nanofluids reveals that a variety of factors influence the nanofluid's final performance. Volume fraction, base fluid, nanoparticle size and shape, and particle movement patterns are among the characteristics.

Many studies have focused on the impact of different nanoparticle kinds on heat transfer. In the classic Blasius problem, Anuar [3] investigated the effects of Al_2O_3, CuO, and TiO_2 particles. Bognar et al. [4] investigated three types of nanofluids, such as alumina (Al_2O_3), titania (TiO_2), and magnetite (Fe_3O_4), in a base fluid of water for viscous nanofluid flow (Sakiadis flow). They concluded that the solid volume percentage has a big impact on fluid flow and heat transfer. When the three types of nanoparticles were compared, the Al_2O_3 had a much higher thermal conductivity. In another study, Bognar et al. [5] utilized similarity analysis and CFD simulation to examine a steady two-dimensional nanofluid flow along a flat surface. Three different nanofluids were studied theoretically and numerically. The impact of a small number of solid particles (up to 4% concentration) on flow and heat transfer properties was investigated. They concluded that when the volume fraction increases, the dimensionless temperature increases because of improved heat transfer. Furthermore, in nanofluid field, the volume fraction is one of the most important factors. Lee et al. [6] demonstrated that when the volume fraction increased, the thermal conductivity increased linearly. Khanafer [7] devised a two-dimensional model to investigate the heat transfer properties of nanofluids inside a frame. Congedo [8] investigated the natural convection flow for Al_2O_3-water nanofluid. Different approaches have been used to examine the solution of nanofluid challenges. Authors have employed the single phase technique in a variety of geometries in the literature, including flat plate, wedge, square channel, circular tube, and flow over cylinder [9], [10], [11].

According to the literature [12], lubricating oils containing nanoparticles (MoS_2, CuO, TiO_2, diamond, etc.) have increased load-carrying capacity, anti-wear, and friction-reduction qualities. These properties made nanofluids particularly appealing for cooling and/or lubricating applications in a variety of industries, including manufacturing, transportation, energy, and electronics, and so on. For example, in compared to water as an absorbing medium, some experimental findings show that using the nanofluid improves collector efficiency in a solar collector [13]. In this study, the influence of a CuO–water nanofluid as the working fluid, on the performance and efficiency of a flat-plate solar collector is experimentally studied. In another application in enhanced oil recovery (EOR), metal oxide nanoparticles (such as CuO,

Fe_2O_3, and NiO) were discovered to be effective in reducing the viscosity of heavy oil [14]. Another use for nanoparticles is to raise the density and viscosity of a gas that has been injected to an oil well for enhanced oil recovery [15]. In this technique, gas flooding mobility is efficiently controlled, improving gas displacement efficiency and oil recovery. On the EOR of heavy oil, for example, several CO_2 nanofluid (CuO nanoparticles saturated with CO_2) core flood studies are carried out. The findings indicate that due to swelling and displacement of heavy oil, the nanoparticles-CO_2 nanofluid recovered 71.30 percent of the heavy oil, which was 13.30 percent greater than a traditional CO_2 core flood. The process is that adding nanoparticles increases both the density and viscosity of CO_2. The viscosity of CO_2 nanofluids was found to be 140 times that of regular CO_2. Bognar and Hriczo [16] examined the ferrofluid flow boundary layer caused by a permeable stretching sheet. They examined the effects of the magnetic field, Reynolds number, and porosity on the velocity and heat fields. They concluded that increasing the stretching, porosity, and ferromagnetic parameter reduces skin friction and heat transfer coefficients. In another numerical study, Bognar and Hriczo [17] studied the steady two-dimensional boundary layer flow across an extending flat sheet in a water-based ferrofluid. In ferrofluid flows along nonlinearly stretched sheets, the effects of volume fraction of solid ferroparticles and non-uniform magnetic field on dimensionless velocity and temperature, as well as the skin friction coefficient and local Nusselt number, were investigated for three selected ferroparticles (magnetite, cobalt ferrite, and Mn-Zn ferrite). They concluded that when the volume fraction increases, the nanofluid flow slows and the temperature increases.

Eastman et al. [18] concluded that a nanofluid made up of water and 5% CuO nanoparticles can improve thermal conductivity by around 60%. Lee et al. [6] showed that CuO particles are smaller than Al_2O_3 particles, implying that CuO-nanofluids have higher thermal conductivity than Al_2O_3-nanofluids. Heris et al. [19] considered a constant temperature boundary condition rather than a constant heat flux condition by flowing saturated steam in a tube. They discovered that increasing the nanoparticle volume fraction and the Peclet number improves the heat transfer coefficient. However, as compared to CuO-water nanofluid, Al_2O_3-water nanofluid demonstrated better improvement in heat transfer coefficient. Sivakumar et al. [20], on the other hand, observed that CuO-water nanofluid had a higher heat transfer coefficient than Al_2O_3-water nanofluid due to the high thermal conductivity of CuO particles. This disagreement might be attributed to changes in the boundary condition, nanoparticle size, and model shape. According to another study, CuO nanoparticles had the highest relative thermal conductivity coefficient thanks to their maximum density, followed by Al_2O_3, ZrO_2, TiO_2, and SiO_2. Al_2O_3 nanoparticles are ranked second after CuO nanoparticles [21]. Peng et al. [22] examined the effect of adding CuO nanoparticles to R113 refrigerant on the flow boiling heat transfer performance of the nanorefrigerant (CuO + R113 combination) within a smooth channel. Their findings revealed that the nanorefrigerant's heat transfer coefficient was higher than that of pure refrigerant, with a maximum improvement of 29.7%. Lu et al. [23] investigated the effect of CuO nanofluids based on water on an open thermo

syphon used in a high-temperature evacuated tabular solar collector (HTC). Nanofluid enhanced the evaporator's thermal performance when compared to water, and it also improved the evaporating heat transfer coefficient by 30%. According to Peyghambarzadeh et al. [24], increasing the concentration of CuO/water nanoparticles improves the model's thermal performance. Zarringhalam et al. [25] observed that a slight amount of CuO nanoparticles in water improves the average heat transfer coefficient significantly. Chein et al. [26] investigated CuO/water and discovered that the thermal improvement obtained by adding nanoparticles to the base fluid is dependent on particle size, shape, Reynolds number, and particle volume percent. In another study, the computer simulation of natural convection in a two-dimensional square cavity filled with a water–CuO nanofluid was carried out [27]. The findings suggest that when the Rayleigh number and the percentage of nanoparticles increase, the heat transfer rate increases independent of the position of the source-sink. These researches show that the presence of nanoparticles in the base fluid improves heat transfer.

The velocity distribution and heat transfer improvement of water-CuO nanofluid in a laminar 2D flow within a horizontal channel are investigated numerically in this study. The influence of the volume fraction on heat transfer, velocity, wall shear stress, skin friction coefficient, and Nusselt number have also been studied along the channel. The model is explained in section 2 along with the governing equations that describe the model. In section 3, the geometry generated, the mesh independency study, and the numerical solution method are presented. Finally, the results are presented in section 4.

2. MODEL DESCRIPTION AND GOVERNING EQUATIONS

2.1. Model description

Figure 1 demonstrates the geometry and the computational domain schematically. The channel's diameter and length have been set at 0.1 m and 2 m, respectively. With a temperature of 275 K and a velocity given by Reynolds numbers equal to 1,000 (Re = 1,000), the flow at the inlet has been assumed to be hydrodynamically steady. The lower wall receives a constant heat flux of 200 W/m^2 from downside, while the upper wall is set to be adiabatic from up. This numerical investigation uses a single-phase technique to solve the nanofluid flow problem. The following assumptions are employed in this approach:

1. The nanoparticles and the base fluid (water) are assumed to be mixed precisely and the whole mixture is regarded homogeneous. In addition, the fluid phase and solid particles are supposed to be in thermal equilibrium and to flow at the same speed.
2. Fluid flow that is steady, Newtonian, and incompressible is considered.
3. The thermophysical properties of nanofluids, such as density, thermal conductivity, viscosity, and thermal conductivity, are temperature independent and completely depend on the nanoparticle volume fraction.
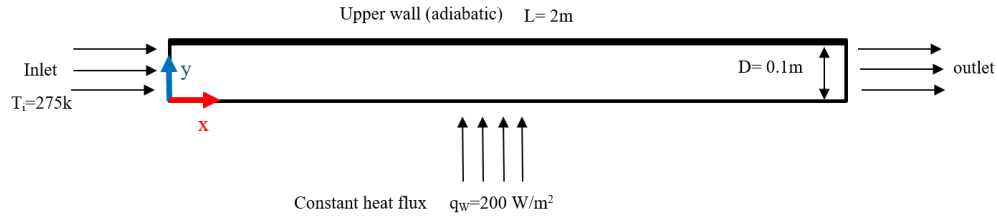
Figure 1. *The schematic diagram of the computational domain*

The wall is made from aluminium and its properties are given in *Table 1*.

<div align="right">

Table 1
</div>

<div align="center">

Properties of wall made from aluminium
</div>

Density, ρ (kg/m^3)	Specific heat, Cp (J/kg K)	Thermal conductivity, k (W/m K)
2,719	871	202.4

2.2. Governing equations

The mathematical formulation of the single-phase model for Newtonian fluid is presented by *Equations (1)* to *(3)*, which are continuity, momentum, and energy governing equations, respectively [28]:

$$\text{div}\left(\rho_{nf}\vec{V}\right) = 0, \tag{1}$$

$$\text{div}\left(\rho_{nf}\vec{V}\vec{V}\right) = -\nabla P + \mu_{nf}\nabla^2\vec{V}, \tag{2}$$

$$\text{div}\left(\rho_{nf}\vec{V}C_{pnf}T\right) = \text{div}(k_{nf}\nabla T). \tag{3}$$

The following notations are used in the above equations:
$\vec{V}$: the velocity vector,
P: the pressure of the nanofluid,
T: the temperature of the nanofluid,
μ_{nf}: the dynamic viscosity of the nanofluid,
ρ_{nf}: the density of the nanofluid is density of the nanofluid,
k_{nf}: thermal conductivity of the nanofluid,
Cp_{nf}: thermal capacity of the nanofluid.

2.3. Thermal properties of the nanofluid

As a function of the volume fraction, the thermal properties of the nanofluid are calculated. By using *Equations (4)–(7)*, the density, thermal capacity, viscosity, and thermal conductivity are estimated based on the concentration of nanoparticles in the base fluid. The effective density of the nanofluid is given by [29]:

$$\rho_{nf} = (1-\varphi)\rho_{bf} + \rho_s\varphi, \tag{4}$$

where, ρ_{bf} and ρ_s refer to the density of base fluid and nanoparticles, respectively. The heat capacity of the nanofluid C_{pnf} is considered to be as below [29], [30]:

$$C_{pnf} = \frac{\varphi(\rho C_p)_s + (1-\varphi)(\rho C_p)_{bf}}{\rho_{nf}}. \tag{5}$$

The viscosity of nanofluid μ_{nf} is obtained from below equation, which is called Brinkman equation as follows [31], [32]:

$$\mu_{nf} = \frac{\mu_{bf}}{(1-\varphi)^{2.5}}, \tag{6}$$

where, μ_{bf} is the viscosity of the base fluid (water), and φ refers to nanoparticle volume fraction.

The thermal conductivity of nanofluid knf is given as follows [33]:

$$k_{nf} = k_{bf}\frac{k_s + 2k_{bf} - 2\varphi(k_{bf} - k_s)}{k_s + 2k_{bf} + \varphi(k_{bf} - k_s)}. \tag{7}$$

where, k_{bf} is the thermal conductivity of base fluid, and k_s is the thermal conductivity of the nanoparticles.

Thermo-physical properties for pure water and various types of nanoparticles are given in *Table 2*, and the thermo-physical properties for CuO-water nanofluid at different values of φ are presented in *Table 3*.

Table 2
Thermo-physical properties for pure water and
various types of nanoparticles [34]

PARTICLE TYPE	ρ (kg/m^3)	μ (N s/m^2)	k (W/m K)	Cp (J/kg K)
Pure water	998.2	0.001003	0.6	4,182
Al_2O_3	3,970	–	40	765
CuO	6,500	–	20	535.6
SiO_2	2,200	–	1.2	703
ZnO	5,600	–	13	459.2

Table 3
Thermo-physical properties for CuO-water at different values of φ
[29],[30],[31],[32], [33]

VOLUME FRACTION (φ)	(1%)	(2%)	(3%)	(4%)
ρ_{nf} (kg/m^3)	1,053.218	1,108.236	1,163.254	1,218.272
C_{pnf} (J/kg K)	3,956.96017	3,754.264391	3,570.74227	3,403.796118
k_{nf} (W/m K)	0.616623822	0.633557563	0.650809972	0.668390129
μ_{nf} (N s/m^2)	0.00102852	0.001054959	0.00108236	0.001110767

3. NUMERICAL PROCEDURE

3.1. Geometry and mesh independency investigation

The geometry is generated by using DesignModeler of official Ansys Fluent, and the two-dimensional flow problem in one-phase was selected. The channel's diameter and length have been set at 0.1 m and 2 m, respectively. The inlet flow temperature was set at 275 K with a velocity given by Reynolds numbers equal to 1,000. The lower wall receives a constant heat flux of 200 W/m^2, while the upper wall is set to be adiabatic. Non-uniform quadrilateral grid system is employed for meshing the domain generated by Meshing of official Ansys Fluent as shown in *Figure 2*. Because the accuracy of finite volume techniques is strongly related to the quality of the discretization utilized, the grid independence test is performed to confirm that the given solution is mesh independent. As a result, a precise mesh sensitivity investigation was conducted in order to reduce the numerical impacts imposed by mesh size. The mesh sensitivity was examined for six meshes, and the test compared the average Nusselt number on the bottom wall for each mesh. The results are shown in *Table 4*. The Nusselt number for mesh 3 with 12,400 cells was determined to be adequate for ensuring the accuracy of the solution as well as the grid's independence.
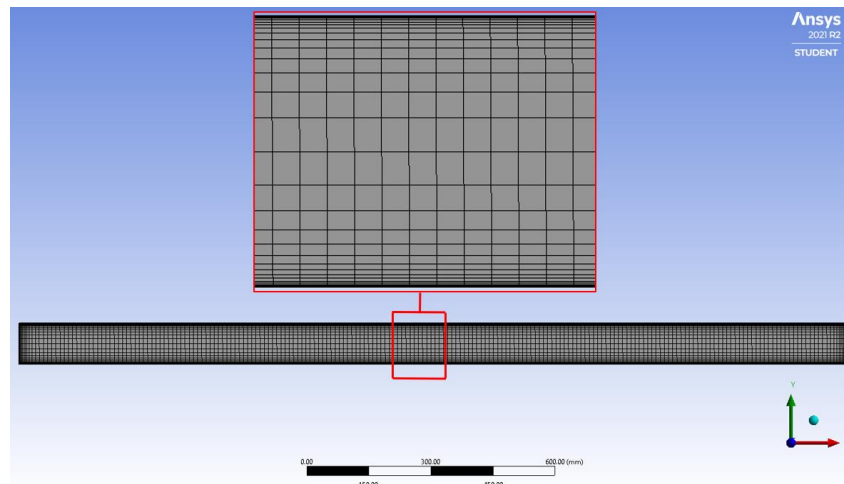

Figure 2. *Mesh generation for the model*

Table 4
Mesh independency investigation

Mesh	Number of cells	Average Nusselt number
1	2,400	23.88086
2	6,390	24.15811
3	**12,400**	**24.25852**
4	20,250	24.30758

3.2. Numerical solution method

The equations of mass, momentum, and energy were discretized using the finite volume method (FVM). The calculations were done using Ansys Fluent Solver, which solved the system of *Equations (1)–(3)* as well as the boundary conditions. The procedure for solving the problem was as follows: A simple algorithm was used to resolve the velocity-pressure coupling. The convection and diffusion terms in the governing equations were discretized using a second-order upwind scheme. The convergence criteria of the solutions monitored by a residual monitor of 10^{-6}.

4. RESULTS

4.1. Contours

4.1.1. Temperature contour of cuo-water nanofluid

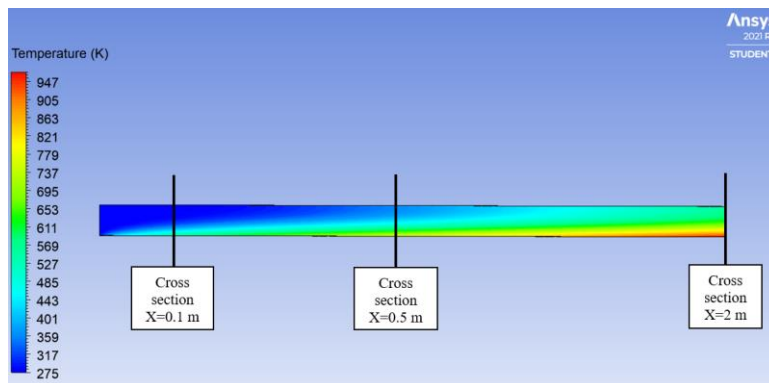The temperature contour for nanofluid containing 4% CuO along the whole channel is presented in *Figure 3*.

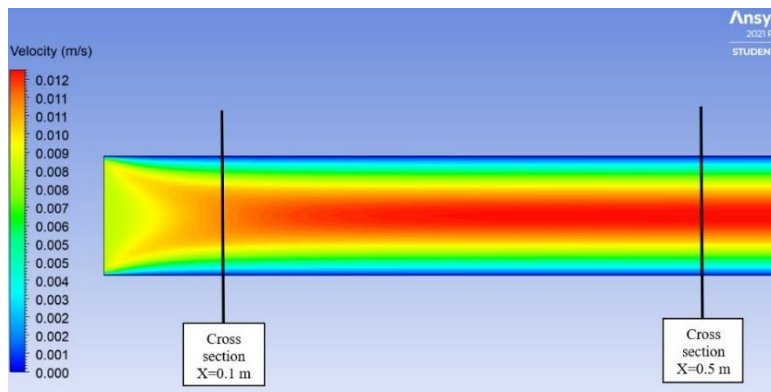**Figure 3.** *Temperature contour for nanofluid containing 4% CuO along the pipe*

Figure 4. *Velocity contour for nanofluid containing 4% CuO along the pipe*

As it is illustrated, the nanofluid enters the channel at temperature equal to inlet temperature (275 K), and the temperature gradually increases as it moves forward along the channel. Due to having a constant heat flux at the lower wall while the upper wall is thermally insulated, the temperature of nanofluid at lower part of the channel specifically near to the lower wall tends to rise. To precisely investigate the thermal behavior of nanofluid, three cross sections along the channel (X = 0.1, 0.5, and 2 m) are selected and will be discussed in part 4.2.

4.1.2. Velocity contour of nanofluid containing cuo

The velocity contour for nanofluid containing 4% CuO along the section of the channel which a fully developed regime was established is presented in *Figure 4*. As it is illustrated, the velocity of nanofluid is not influenced by the thermal conditions at lower and upper walls, and it is only affected by the nanoparticle volume fraction. It is shown that the velocity near the walls is equal to zero due to no slip condition between walls and nanofluid. The velocity distribution along the channel is worthwhile to be studied. Therefore, two cross sections along the channel (X = 0.1 and 0.5 m) are selected and will be discussed in part 4.3.

4.2. Thermal effect of nanofluid containing CuO

Numerical results for the thermal boundary layers at different locations along the channel are presented. *Figure 5* depicts the impact of nanoparticle volume fraction on the temperature profile for CuO-water nanofluid flow at three different cross sections (X = 0.1, 0.5, and 2 m) along the channel.
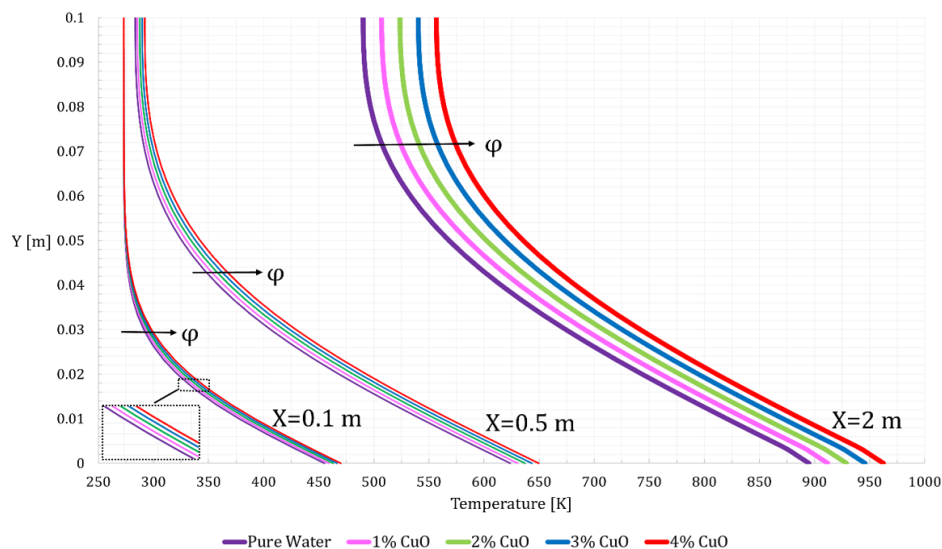

Figure 5. *Temperature distribution at different cross sections for different nanoparticle volume fractions*

The Y-axis shows diameter of the channel while the X-axis shows temperature. Thermal boundary layer thickness increases with an increase in the parameter φ which is nanoparticle volume fraction. Comparison of the temperature profiles for different nanofluid concentrations shows that CuO-water at 4% has the thickest thermal boundary layer. Therefore, it is observed that the nanoparticles change the flow and heat transfer characteristics and causes an increase in the thermal boundary layer. Moreover, the graph shows that the temperature near the lower wall at cross section X = 0.1m is around 475 K while it rises to 650 K and 950 K at cross sections X = 0.5m and X = 2m, respectively. This is due to existence of a constant heat flux at the bottom wall along the channel when the nanofluid reaches the end of the channel, it receives more heat from the lower wall. However, the increase of temperature near the upper wall along the channel length is not as rapid as that of for the lower wall since the upper wall is thermally insulated and is receiving heat only from the nanofluid flowing inside the channel.

4.3. Hydrodynamic effect of nanofluid containing CuO

The velocity distributions of nanofluid for nanoparticle volume fractions φ = 1, 2, 3, and 4% of CuO with the inlet Reynold's number Re = 1,000 at cross sections X = 0.1m and X = 0.5 m along the channel are shown in *Figures 6–7*. The numerical simulations reveal that when the volume fraction increases, the velocity of nanofluid increases. Therefore, the volume fraction has an impact on the nanofluid's velocity, as shown by the results. It is shown that the maximum velocity of nanofluid happens at nanoparticle volume fraction equal to 4%. It can be observed from *Figure 6* that the velocity profile at cross section X = 0.1 has not arrived the fully developed regime yet; however, there is a fully developed regime at cross section X = 0.5 in *Figure 7*.
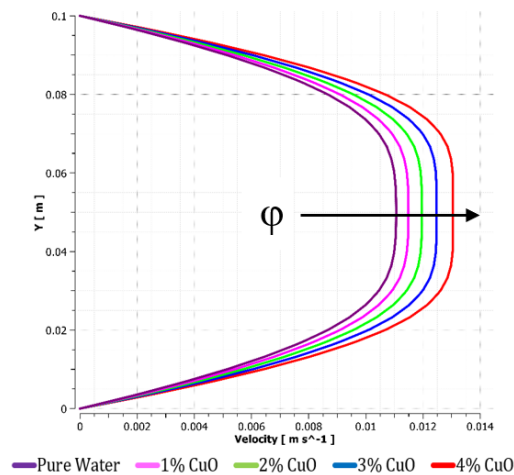

Figure 6. *Velocity distribution for different nanoparticle volume fractions at cross section X = 0.1 m*
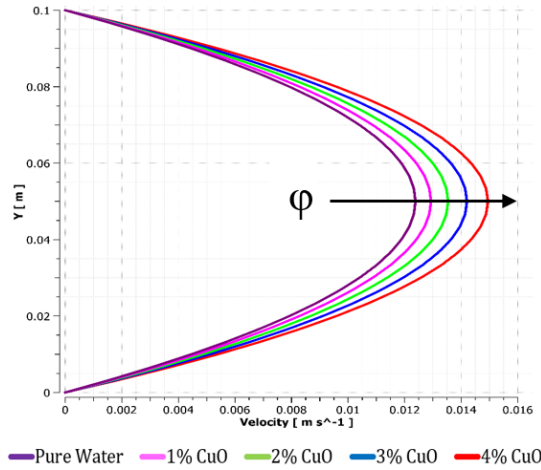
Figure 7. *Velocity distribution for different volume fractions
at cross section X = 0.5* m

The wall shear stress and skin friction coefficient are both of engineering importance and will be shown and examined in detail. The wall shear stress (τ_w) and heat flux (q_w) are defined as

$$\tau_w = \mu_{nf}\left(\frac{\partial u}{\partial y}\right)_{y=0}, \qquad q_w = -k_{nf}\left(\frac{\partial T}{\partial y}\right)_{y=0}, \tag{8}$$

while the skin friction coefficient (C_f) and the local Nusselt number (Nu) are defined as

$$C_f = \frac{\tau_w}{\rho_{nf}U^2}, \; Nu = \frac{x\,q_w}{k_{nf}(T_w - T_{nf})}. \tag{9}$$

Figure 8 shows the influence of the volume fraction on the wall shear stress along the channel's lower wall.
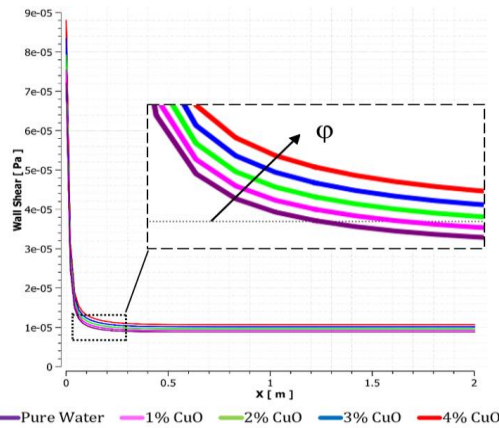

Figure 8. *Wall shear stress at different volume fractions along the lower wall of pipe*

As it is shown, when the volume fraction of CuO nanoparticles increases, the value of the wall shear stress along the bottom wall increases. It shows that nanoparticle volume fraction has an impact on wall shear stress along the channel. Nanofluid with 4% of nanoparticle concentration has the highest amount of wall shear stress along the channel.

Figure 9 and *10* show the influence of the volume fraction on the skin friction coefficient and Nusselt number along the channel's lower wall. As it is shown, when the volume fraction of CuO nanoparticles increases, the value of the skin friction coefficient and Nusselt number along the bottom wall increases. It shows that nanoparticle volume fraction has an impact on skin friction coefficient and Nusselt number along the channel. Nanofluid with 4% of nanoparticle concentration has the highest amount of skin friction coefficient as well as Nusselt number along the channel.
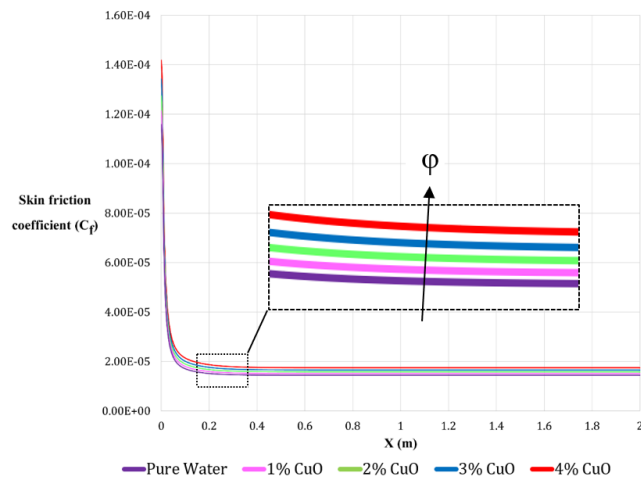

Figure 9. *The skin friction coefficient at different volume fractions along the lower wall of pipe (it would be enough in the range of 0 and 8 10^{-5})*
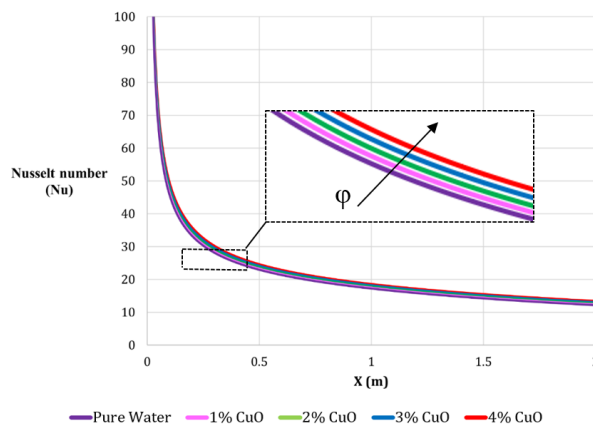

Figure 10. *Nusselt number at different volume fractions along the lower wall of pipe*

5. CONCLUSION

Nanofluid flow within a horizontal channel was numerically investigated using CFD simulation. The influence of CuO nanoparticles on water base fluid has been highlighted in this work. It has been examined how the velocity distribution, the wall shear stress, skin friction coefficient, the temperature distribution, and Nusselt number vary with volume fraction of the nanoparticles. The maximum velocity shows an increase with increasing volume fraction. It is obtained that the temperature increased with increasing the volume fraction of CuO everywhere along the channel. Moreover, it is observed that when the volume fraction increases, the wall shear stress and skin friction coefficient, and Nusselt number along the channel increase as well. The goal is to see how the concentration of nanoparticles affects the velocity and temperature profiles of nanofluid flow in a horizontal channel. Further study is recommended in the transition and turbulent flow for the same model.

REFERENCES

[1] Hussein, A. M. – Bakar, R. A. – Kadirgama, K. – Sharma, K. V. (2013). Experimental measurement of nanofluids thermal properties. International Journal of Automotive and Mechanical Engineering, Vol. 7, No. 1. http://doi.org/10.15282/ijame.7.2012.5.0070

[2] Choi, S. U. S. (1995). *Enhancing thermal conductivity of fluids with nanoparticles*. American Society of Mechanical Engineers, Fluids Engineering Division (Publication) FED, Vol. 231. No. 1995.

[3] Anuar, N. S. – Bachok, N. (2016). Blasius and Sakiadis Problems in Nanofluids using Buongiorno Model and Thermophysical Properties of Nanoliquids. *European International Journal of Science and Technology*, Vol. 5, No. 4.

[4] Bognár, G. – Klazly, M. – Hriczó, K. (2020). Nanofluid flow past a stretching plate. *Processes*, Vol. 8, No. 7, 827, https://doi.org/10.3390/pr8070827.

[5] Bognár, G. – Klazly, M. – Mahabaleshwar, U. S. – Lorenzini, G. – Hriczó, K. (2021). Comparison of Similarity and Computational Fluid Dynamics Solutions for Blasius Flow of Nanofluid. *Journal of Engineering Thermophysics*, Vol. 30, No. 3, pp. 461–475, http://doi.org/10.1134/s1810232821030103.

[6] Lee, S. – Choi, S. – Li, S. – Eastman, J. (1999). Measuring Thermal Conductivity of Fluids Containing Oxide Nanoparticles. *Heat Transfer*, Vol. 121, No. 1999, http://doi.org/10.1115/1.2825978.

[7]   Khanafer, K. – Vafai, K. – Lightstone, M. (2003). Buoyancy-driven heat transfer enhancement in a two-dimensional enclosure utilizing nanofluids. *International Journal of Heat and Mass Transfer*, Vol. 46, No. 19. http://doi.org/10.1016/S0017-9310(03)00156-X

[8]   Congedo, P. M. – Collura, S. – Congedo, P. M. (2009). Modeling and analysis of natural convection heat transfer in nanofluids. *2008 Proceedings of the ASME Summer Heat Transfer Conference*, HT 2008, Vol. 3. http://doi.org/10.1115/HT2008-56289

[9]   Bianco, V. – Nardini, S. – Manca, O. (2011). Enhancement of heat transfer and entropy generation analysis of nanofluids turbulent convection flow in square section tubes. *Nanoscale Research Letters*, Vol. 6, No. 1. http://doi.org/10.1186/1556-276X-6-252

[10]   Yacob, N. A. – Ishak, A. – Pop, I. – Vajravelu, K. (2011). Boundary layer flow past a stretching/shrinking surface beneath an external uniform shear flow with a convective surface boundary condition in a nanofluid. *Nanoscale Research Letters*, Vol. 6, No. 1, http://doi.org/10.1186/1556-276X-6-314.

[11]   Bianco, V. – Chiacchio, F. – Manca, O. – Nardini, S. (2009). Numerical investigation of nanofluids forced convection in circular tubes. *Applied Thermal Engineering*, Vol. 29, No. 17–18. http://doi.org/10.1016/j.applthermaleng.2009.06.019

[12]   Verma, A. – Jiang, W. – Abu Safe, H. H. – Brown, W. D. – Malshe, A. P. (2008). Tribological behavior of deagglomerated active inorganic nanoparticles for advanced lubrication. *Tribology Transactions*, Vol. 51, No. 5. http://doi.org/10.1080/10402000801947691

[13]   Moghadam, A. J. – Farzane-Gord, M. – Sajadi, M. – Hoseyn-Zadeh, M. (2014). Effects of CuO/water nanofluid on the efficiency of a flat-plate solar collector. *Experimental Thermal and Fluid Science*, Vol. 58. http://doi.org/10.1016/j.expthermflusci.2014.06.014

[14]   Patel, H. – Shah, S. – Ahmed, R. – Ucan, S. (2018). Effects of nanoparticles and temperature on heavy oil viscosity. *Journal of Petroleum Science and Engineering*, Vol. 167, http://doi.org/10.1016/j.petrol.2018.04.069.

[15]   Shah, R. D. (2009). App1ication of nanoparticle saturated injectant gases for EOR of heavy oils. *Proceedings SPE Annual Technical Conference and Exhibition*, Vol. 7, http://doi.org/10.2118/129539-STU.

[16]   Bognár, G. – Hriczó, K. (2020). Ferrofluid flow in magnetic field above stretching sheet with suction and injection. *Mathematical Modelling and Analysis*, Vol. 25, No. 3, pp. 461–472, http://doi.org/10.3846/mma.2020.10837.

[17]   Bognár, G. – Hriczó, K. (2020). Numerical Simulation of Water Based Fer-rofluid Flows along Moving Surfaces. *Processes*, Vol. 8, No. 7, p. 830. http://doi.org/10.3390/pr8070830

[18]   Eastman, J. A. – Choi, U. S. – Li, S. – Thompson, L. J. – Lee, S. (1997). En-hanced thermal conductivity through the development of nanofuids. *Nanophase and Nanocomposite Materials II*, http://doi.org/10.1557/PROC-457-3.

[19]   Heris, S. Z. – Etemad, S. G. – Esfahany, M. N. (2006). Experimental investi-gation of oxide nanofluids laminar flow convective heat transfer. *Interna-tional Communications in Heat and Mass Transfer*, Vol. 33, No. 4. http://doi.org/10.1016/j.icheatmasstransfer.2006.01.005

[20]   Sivakumar, A. – Alagumurthi, N. – Senthilvelan, T. (2016). Experimental in-vestigation of forced convective heat transfer performance in nanofluids of Al2O3/water and CuO/water in a serpentine shaped micro channel heat sink. *Heat and Mass Transfer/Waerme- und Stoffuebertragung*, Vol. 52, No. 7. http://doi.org/10.1007/s00231-015-1649-5

[21]   Rudyak, V. Y. – Belkin, A. A. – Tomilina, E. A. (2010). On the thermal con-ductivity of nanofluids. *Technical Physics Letters*, Vol. 36, No. 7. http://doi.org/10.1134/S1063785010070229

[22]   Peng, H. – Ding, G. – Jiang, W. – Hu, H. – Gao, Y. (2009). Heat transfer characteristics of refrigerant-based nanofluid flow boiling inside a horizontal smooth tube. *International Journal of Refrigeration*, Vol. 32, No. 6. http://doi.org/10.1016/j.ijrefrig.2009.01.025

[23]   Lu, L. – Liu, Z. H. – Xiao, H. S. (2011). Thermal performance of an open thermosyphon using nanofluids for high-temperature evacuated tubular solar collectors. Part 1: Indoor experiment, *Solar Energy*, Vol. 85, No. 2. http://doi.org/10.1016/j.enconman.2013.04.010

[24]   Peyghambarzadeh, S. M. – Hashemabadi, S. H. – Chabi, A. R. – Salimi, M. (2014). Performance of water based CuO and Al2O3 nanofluids in a Cu-Be alloy heat sink with rectangular microchannels. *Energy Conversion and Man-agement*, Vol. 86, http://doi.org/10.1016/j.enconman.2014.05.013.

[25]   Zarringhalam, M. – Karimipour, A. – Toghraie, D. (2016). Experimental study of the effect of solid volume fraction and Reynolds number on heat transfer coefficient and pressure drop of CuO-Water nanofluid. *Experimental Thermal and Fluid Science*, Vol. 76. http://doi.org/10.1016/j.expthermflusci.2016.03.026

[26]   Chein, R. – Chuang, J. (2007). Experimental microchannel heat sink perfor-mance studies using nanofluids. *International Journal of Thermal Sciences*, Vol. 46, No. 1, http://doi.org/10.1016/j.ijthermalsci.2006.03.009.

[27] Aminossadati, S. M. – Ghasemi, B. (2011). Natural convection of water-CuO nanofluid in a cavity with two pairs of heat source-sink. *International Communications in Heat and Mass Transfer*, Vol. 38, No. 5. http://doi.org/10.1016/j.icheatmasstransfer.2011.03.013

[28] Alrashed, A. A. A. A. et al. (2018). The numerical modeling of water/FMWCNT nanofluid flow and heat transfer in a backward-facing contracting channel. *Physica B: Condensed Matter*, Vol. 537. http://doi.org/10.1016/j.physb.2018.02.022

[29] Khanafer, K. – Vafai, K. (2011). A critical synthesis of thermophysical characteristics of nanofluids. *International Journal of Heat and Mass Transfer*, Vol. 54, No. 19–20, http://doi.org/10.1016/j.ijheatmasstransfer.2011.04.048.

[30] Xuan, Y. – Li, Q. (2000). Heat transfer enhancement of nanofluids. *International Journal of Heat and Fluid Flow*, Vol. 21, No. 1. http://doi.org/10.1016/S0142-727X(99)00067-3

[31] Mahbubul, I. M. – Saidur, R. – Amalina, M. A. (2012). Latest developments on the viscosity of nanofluids. *International Journal of Heat and Mass Transfer*, Vol. 55, No. 4, http://doi.org/10.1016/j.ijheatmasstransfer.2011.10.021.

[32] Abu-Nada, E. (2008). Application of nanofluids for heat transfer enhancement of separated flows encountered in a backward facing step. *International Journal of Heat and Fluid Flow*, Vol. 29, No. 1, pp. 242–249. http://doi.org/10.1016/j.ijheatfluidflow.2007.07.001

[33] Kakaç, S. – Pramuanjaroenkij, A. (2009). Review of convective heat transfer enhancement with nanofluids. *International Journal of Heat and Mass Transfer*, Vol. 52, No. 13–14, http://doi.org/10.1016/j.ijheatmasstransfer.2009.02.006.

[34] Kherbeet, A. S. – Mohammed, H. A. – Salman, B. H. (2012). The effect of nanofluids flow on mixed convection heat transfer over microscale backward-facing step. *International Journal of Heat and Mass Transfer*, Vol. 55, No. 21–22, http://doi.org/10.1016/j.ijheatmasstransfer.2012.05.084.

CONTACT PATTERN INVESTIGATION OF GEAR DRIVES USING FINITE ELEMENT METHOD

ÁDÁM SÁNDOR PINTÉR[1] – FERENC SARKA[2]

[1]*University of Miskolc, Institute of Machine Tools and Mechatronics*
3515 Miskolc-Egyetemváros
pinter.adam.1998@gmail.com
https://orcid.org/0000-0002-6555-3664

[2]*University of Miskolc, Institute of Machine and Product Design*
3515 Miskolc-Egyetemváros
machsf@uni-miskolc.hu
https://orcid.org/0000-0003-3136-4248

Abstract: This article deals with a study that examines deviations in the curve generated by CAD software and real involutes. As part of this, FEM tests are carried out further from the conclusions drawn from the deviations of the gears created, the purpose is to determine the contact pattern at the design stage. Furthermore, using the results of the studies, we can determine how accurately our results give an accurate picture compared to the result that can be calculated from the theory. Finally, we also test for shafts deformation in the connection of the gears.

Keywords: gears, CAD model, FEM analysis, mounting defects

1. INTRODUCTION

Gear drives cover a very significant area in traditional mechanical engineering. The aim of the authors of this article is to create a method based on CAD and FEM software, with which the examination of the contact pattern of gear drives can be carried out during the design phase. For each FEM test, it is necessary to create a CAD model. In this article, we will briefly summarize the shape difference of the toothed elements generated by CAD software compared to the theoretical (involut) tooth profile. From this we make a decision whether these gears can be used for FEM testing. If the difference is is too large, we only get a right result during the FEM test if we create the gear ourselves. After that, we create a CAD model that presents a gear drive. Steps to create this proper gear are described in detail. In addition, we perform the FEM test and determine how much the results obtained give a true picture compared to the theoretical values described in standards. We also create a model that shows a gear drive with shafts, and we also carry out tests on this to see what problems the deformation of shafts can cause during real operation.

2. COMPARISON OF TOOTH PROFILES OBTAINED FROM CAD SYSTEM WITH THEORETICAL INVOLUTE [1]

CAD systems currently in use have a predefined program module for making built-in toothed elements. However, we do not know how realistic the gears generated in this way are and how much the curve describing the tooth profile corresponds to the theoretical involute. Thus, we need to consider whether they are only for visual display or give back the tooth profile completely correctly. It is determined that for the test we will use a gear with a 20 tooth number and a module of 3 mm [1]. The CAD system we use is Solid Egde, in this software the gear model is made. We also used an MS excel table to draw, in which we calculate each control points of the involute curve. The finished model is shown in *Figure 1*. Here you will also see the construction lines used for drawing, which are made up of the geometry of the gear.
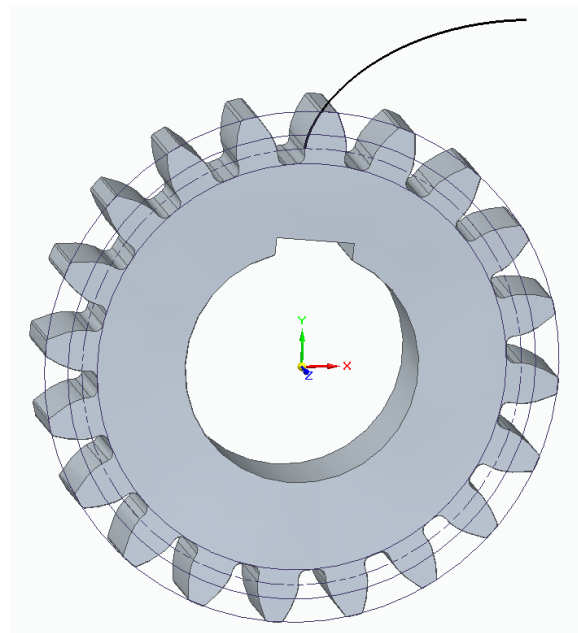

Figure 1. *The model of the finished gear* [1]

After that, with the help of the built-in module, we create the generated gears. For this we also use Solid Edge. To have a different software, we also create the gear with Inventor's module. We make tests on the tooth profile, with visual inspection in first approach. Here we place the teeth side by side in a comparison picture, covering them with the gear we have drawn. The result is illustrated in *Figure 2*, which shows the differences in the different tooth profiles of different softwares. In the figures, the grayed tooth profile shows the tooth of the gear we generate, and the green color shows the profile generated by the software.
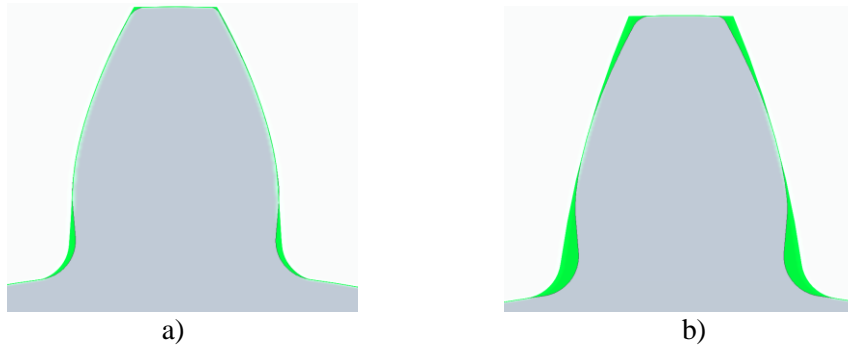
a)   b)

Figure 2. *a) Comparison-Solid Egde, b) Comparison-Inventor*

As shown in *Figure 2*, there are differences between the tooth profiles of the gears. The values of this can also be determined [1]. Furthermore, we can perform the test by changing the values of the module and examining the differences in these gears. In our case, we create gears ranging from a 1 mm module to a 5 mm module, on which we measure the deviation values at the topland and the pitch circle. The measured deviations for gears created in Solid Edge are shown in *Table 1*. We only noticed a deviation at topland, so we can see its percentage evaluation.

Table 1

Differences in gears generated by Solid Edge

Module value	Drawn by us	CAD generated	Variance
1 mm	0.693 mm	0.701 mm	1.15%
2 mm	1.386 mm	1.403 mm	1.22%
3 mm	2.075 mm	2.105 mm	1.44%
4 mm	2.773 mm	2.806 mm	1.19%
5 mm	3.465 mm	3.508 mm	1.24%

The difference between the gear created by Inventor and the wheel we create is summarized in *Table 2*. It must be said here that, as in the previous case, there was only a difference in the point taken at the topland.

Table 2

Differences in gears generated by Inventor

Module value	Drawn by us	CAD generated	Variance
1 mm	0.693 mm	0.869 mm	25.3%
2 mm	1.386 mm	1.727 mm	24.6%
3 mm	2.075 mm	2.591 mm	24.8%
4 mm	2.773 mm	3.454 mm	24.5%
5 mm	3.465 mm	4.318 mm	24.6%

Here the question arises as to what is the difference that can still be allowed if we want to carry out a finite element analysis with them. Both models may be available for some tasks, but a small deviation in Solid Edge may be a problem in other tests. We have to examine this further to how much deviation may affect our results. In conclusion, it can be said that if we already know the process of the solution, how to draw involute curves from calculated results in CAD systems, and we have such experience, it may be better to design and produce the gear model by us, because this way we will surely get the right result.

3. PREPARATION OF GEARS IN CAD SYSTEM FOR FEM TESTING

In order to use the CAD model to test contact surfaces, we need to rotate the two gears. Here we use the gears we make. The next step is that to position the two gears, you will need an auxiliary part. In their case, it will be a plate, which will also be drawn in Solid Edge. In the ISO metric assembly module, we load in our drawn plate. On the plate we apply the center distance of the two gears, based on the calculation 60 mm. At a distance corresponding to the center distance, a hole is drawn on the plate. If this is the case, we will insert two gears into our assembly. Use the *Add Component* icon here. When we were done with this, we will start to put the parts together with the help of constraints. On the plate, using the *Mate* command and selecting one of the planes of the gear, we fit it to the plane of the plate. This puts them on the same plane, but in order to be in the correct hole, use the *Insert* command. Selecting the center line of the hole and the center line of the gears creates a connection between them. The finished model is shown in *Figure 3*. A paralell keyway has also been drawn in the holes of the gears to make the gear position more noticeable during rotation.
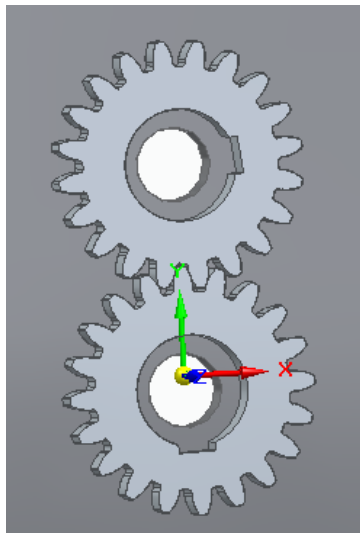

Figure 3. *Finished assembly in Solid Edge*

In the finished assembly, we still need to find the tooth connection in order to simulate physical operation and thus save more CAD models for the FEM software. Thus, in the first step, with the help of the *Move Components* command, we approach the position where the teeth are almost connected. It is important to do this within the *No Analysis* setting. When we are almost in the position of tooth connection, we turn on the *Physical Operation* option, which simulates that the driveer gear (the pinion), in this case the upper gear, drives the driven gear, which means that it becomes the lower gear. The setting can be observed in *Figure 4*.
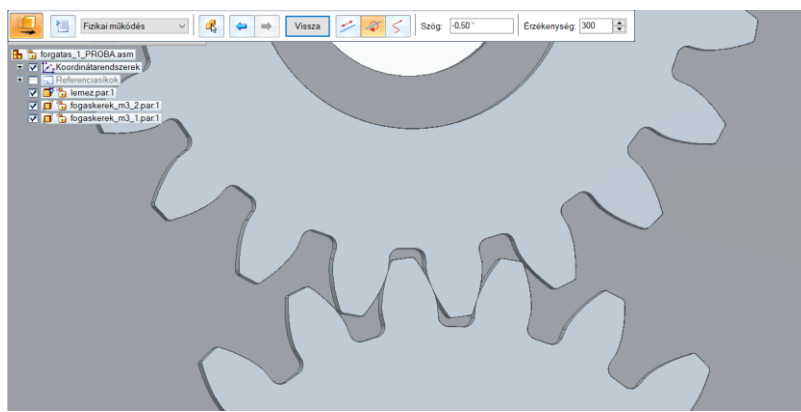


Figure 4. *Set up simulation of physical operation*

With the help of this command, we perform the rotation every half degree. We save each state separately in an intermediate format. This format is the STEP format, which can also be managed by FEM software. With the help of states saved in the intermediate file format, we can already start running FEM analyses. To do this, we use the free student version of the Ansys software used in the Institute.

4. A FEM TEST FOR GEAR CONTACT

Therefore, to perform the test, we use the R2 version of Ansys 2021. After launching the program, which is Workbench, we need to create what kind of test we want to do. Here we choose static structural and create it. Once created, the test status bar is displayed to see what steps need to be taken to complete the simulation. This can be seen in Figure 5. The first step is to create geometry. Here, of course, we read the previously saved STEP format model.

Figure 5
The first step of the FEM investigation
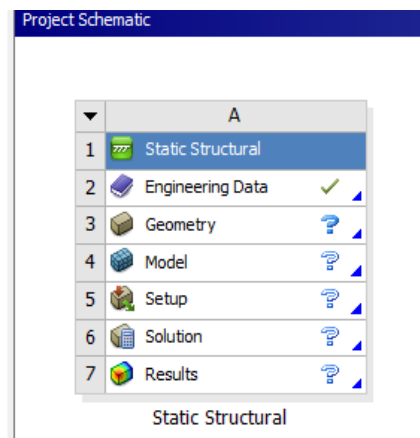
After read the geometry, double-clicking on the model tab will start the AnsysWB Module. In it we can create the details of the analisys. First of all, the auxiliary plate is turned off from our geometry so that it does not participate in the analysis, since it does not affect the connection of the teeth, so we do not tie up unnecessary computational capacity. You can do this by selecting the disk part on the *Geometry* tab and right-clicking it with *Suppress body* command. This part also disappears from display. After that, meshing should be carried out. On the *Mesh* tab, you can create it by command *Generate mesh*. The finished mesh is shown in *Figure 6*. Here we keep the mesh created by the program, and we go on with it.
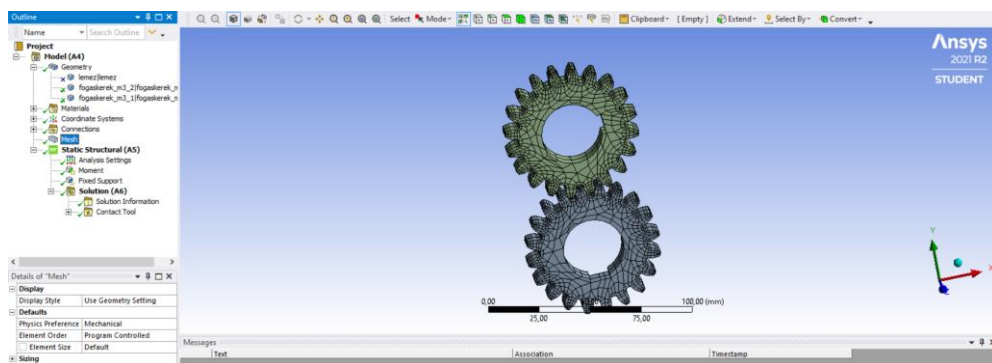

Figure 6. *The finished meshing without the auxiliary plate*

The next step in the *Static Structural* tab is to determine the various constraints and forces, with one expression, the boundary conditions. In our case, we put a torque on the upper gear, which gives us the drive by selecting the inner surface of the hole and operating the torque of 300 Nm on it. However, in order to create a load on the tooth, the driven gear must be braked. To do this, a constraint called *Fixed support* is used, which is determined on the surface of the hole of the lower gear. This step is shown in *Figure 7*. The torque is marked with an arrow, showing which direction it acts in, and highlighting in red the surface on which it is operated. In blue, it represents the fixed support.
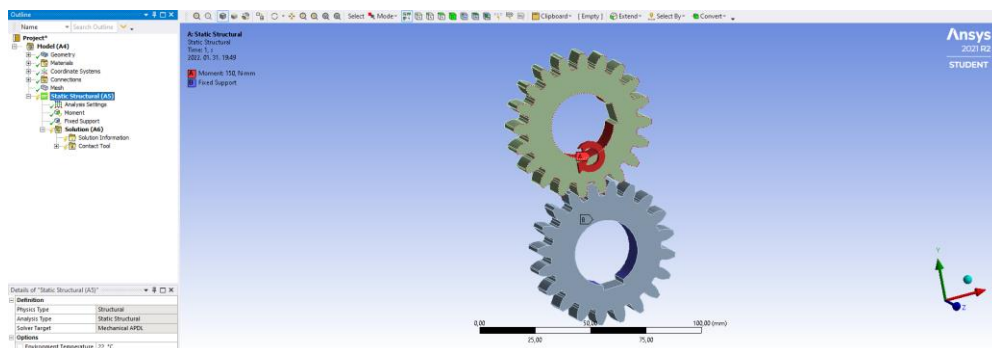

Figure 7. *Description of created constraints*

After the constraints are determined, the solution can be created. Here, by clicking on the *Solution* tab, we can use the *Contact Tool* to get the results of various connection tests. The most important thing for us now is to see these results. The solution is obtained by running the analysis. Thus, by clicking *Solve*, the results are calculated. The result is shown in *Figure 8*.
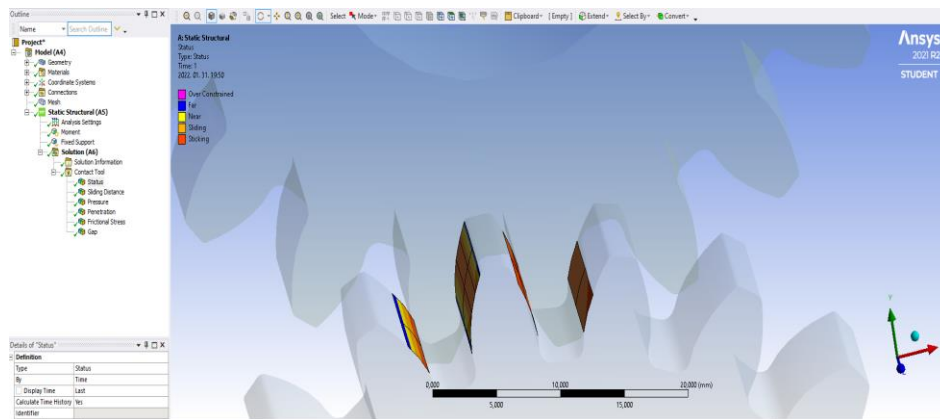

Figure 8. *The result obtained for connecting teeth*

The result clearly shows the connection between the teeth. For us, the important information is given by the yellow and orange color. This is where the connection is made. The yellow color is the *Near* range, where the teeth are close enough to each other to make the connection. And the bright orange is the *Sliding* range, where the two teeth slide on each other. In essence, it is these two areas that provide the contact pattern image. The analysis shows that there is a striped character that meets our expectations, because the connection with these teeth is formed along a line. However, a result was also achieved that presents a flaw. The connection appears on both sides of the tooth. With the correct gear connection, the connection should only appear on the loaded tooth side. From this result we can say that the calculated center distance is 60 mm, but in practice this is not appropriate, as this creates a connection without a clearance. So, it is necessary to change the center distance in order to create the backlash. Thus, it is necessary to modify the CAD model.

5. MODIFICATION OF THE CAD MODEL USING SHAFTS

Since FEM analysis revealed that the theoretical center distane is not connected to the teeth correctly, we have to go back to the model to make modifications on it. If we return to the CAD model, we will further develop the model to simulate the effect of deformation of the elements associated with the gears with the help of the FEM program. We create two shafts on which we can fit the gears. However, the gears will not go to the center of the shafts, but to the third distance of the shaft. Therefore, we expect the result to be a change in the contact pattern image described in the standard. The modified CAD mounting model can be seen in *Figure 9*.
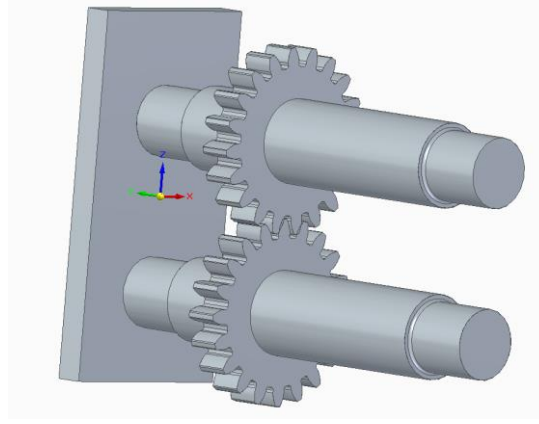
Figure 9. *The modified CAD model*

In the modified CAD model, it is also possible to rotate during physical operation. It is carried out with the difference that in this case we rotate not the center line of the hole, but along the center line of the shaft. We save the models with a half-degree rotation, in intermediate STEP format, similar to the previous one.

6. FEM TEST OF THE SHAFT-MOUNTED GEARS

The initial steps of the study are similar to the previous case. In the same way, we perform a Static Structural test and read the geometry as described above. The auxiliary plate is also turned off (supressed) here so that it does not participate in the simulation. The first deviation in settings can be found in the *Connection* tab. In this case, the contact between the two teeth is set to *Frictional* type, which allows us to specify that there is rolling and sliding between the two teeth at the same time, which is also present in a real gear drive. This value is set to $\mu = 0.05$, which between sliding and rolling. The setting you have made is shown in *Figure 10*.
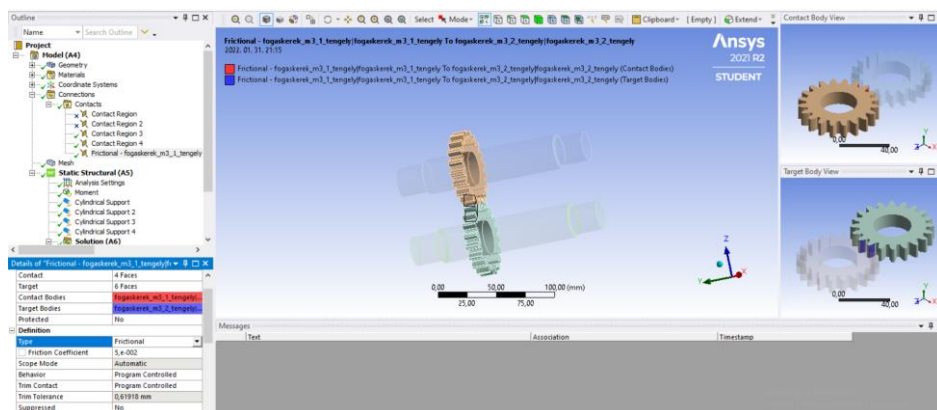

Figure 10. *Taking into account the impact of sliding and rolling*

The next is to set the constraints on the Static Structural tab. Since we have already created an axis here, we will not put the torque on the gear, but will put it on the shaft. Thus, the torque will be transferred through the shaft from one gear to the other gear. The supports are also different in this model. Here *cylindrical support* is applied to the shaft steps, essentially, where bearings would be located in the case of a geardrive. In the case of the drive shaft, the two supports must be allowed to rotate so that they can drive the driven gear and shaft. Thus, in the settings, in the constraint, it is possible to specify whether the radial, axial, and tangential directions are fixed or free of the type of displacement. In the case of the drive shaft, we allow the tangential direction to rotate, but not in the other two directions. This setting is shown in *Figure 11*.

Figure 11. Use of constraints
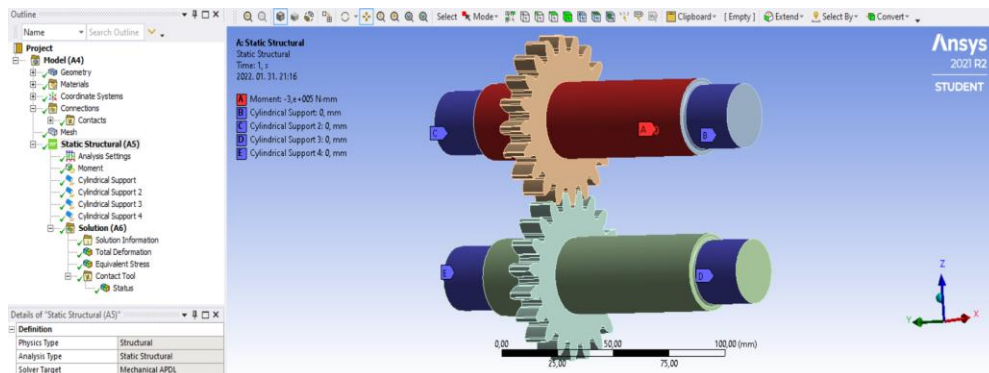
Now we can run the analysis solution. The solution can be examined in *Figure 12*. It can be seen that, as described in the standard, the contact zone is deformed [6]. On one side appears a more compressed area, formed due to the asymmetric distribution of the load. So the FEM analysis returned the result we expected.
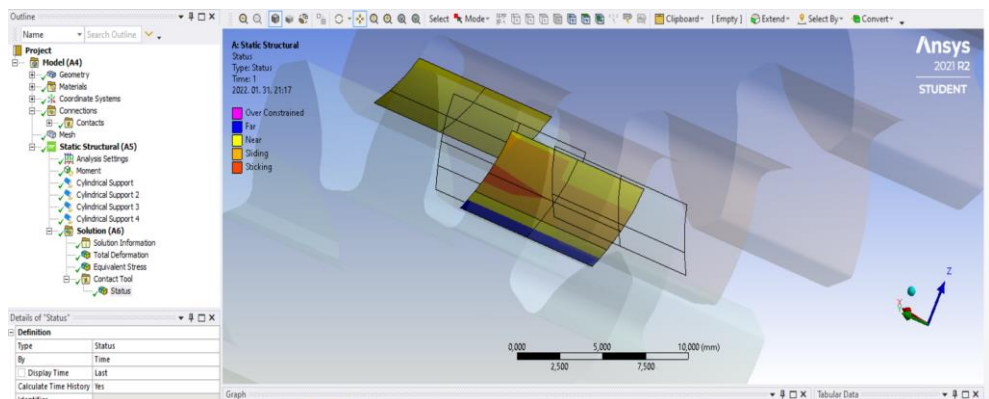

Figure 12. Distortion of the bearing area in case of installation error

7. FORMATION OF THE CONTACT PATTERN BY SUMMING UP SEVERAL ANGULAR POSITIONS

In order to determine the contact pattern and its change, the analysis test presented above must be carried out in several angled situations. By placing these situations next to each other, you can see how the position of the connection line will change depending on the rotation. So we also perform tests on STEP geometries that were previously saved every half degree. These simulations are carried out on a gear connection mounted on the shaft, taken later. The first position is started from a relationship where just one pair of teeth connected. A picture of the initial position is shown in *Figure 13*.
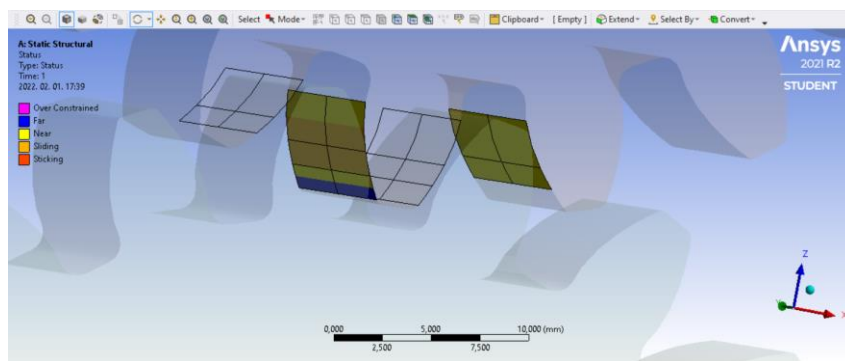

Figure 13. Initial position of meshing-one tooth pair in contact

The next step is to move forward with relationships. However, what we achieve in a position where two teeth connections would already be established, the analysis indicates an error. This is due to the fact that the value of clearance is already less than the element size of the mesh, so the FEM program will detect more connections and will not give us real results. We need to find an opportunity to solve this problem. The solution is to thicken the gear mesh to such a size that the size of the tooth gap does not cause problems. We can do this on the *Mesh* tab, using the *Sizing* command. Here we select our two gears and adjust the size of the mesh to 0.015 mm. This puts us below the value of the tooth gap. A picture of the completed, reduced-size meshing can be seen in *Figure 14*.
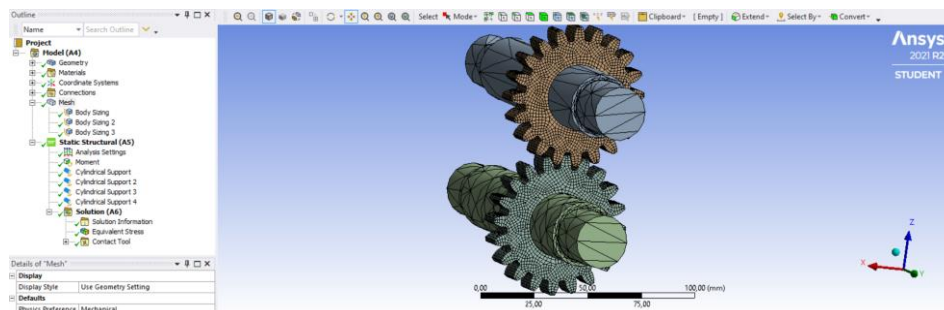

Figure 14. Compressed meshing

Thus, everything is already given to be able to take the contact pattern picture and its change after each turn. In *Figure 15* we can see a change in this displacement, starting from the one tooth relationship, then the entry of the two teeth connections and finally again when only one tooth will be connected. Stress values can also be observed that just when a tooth is in contact, the stress value is distributed on that one tooth, but if two teeth are already connected, the stress value per tooth will decrease.
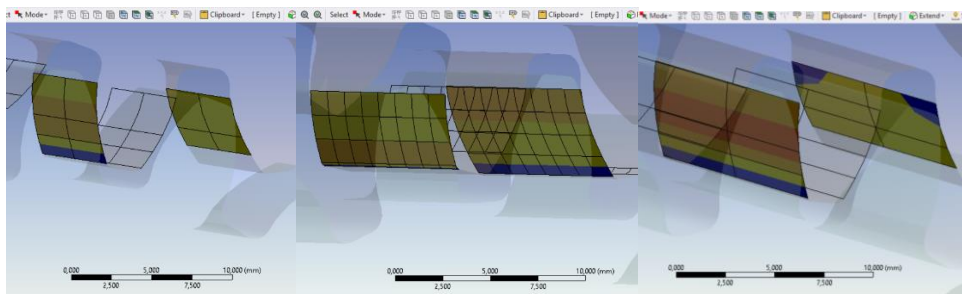

Figure 15. *Change of the contact pattern during rotation*

8. SUMMARY

In the publication, we prepared the involute section for the theoretical tooth profile and used it to draw the gear. Tests were carried out to see how well the gear generated by CAD systems matched the profile of the theoretically accurate gear. In addition, we have created the installations necessary to be able to perform tests with FEM software. During the study, we created two CAD models that are suitable for physical operation, thus providing the basis for the examination of FEM analysis. During the test, it was determined that the theoretical center distance is inadequate, so its value needs to be corrected. We also conducted a study in which we observed the evolution of the contact zone, if we did not just introduce the gears themselves into the CAD model. The effect of the design on the contact zone, and through this on the contact pattern image, can be detected already during the design phase, and already at this stage we can make observations about how the connection will develop in the case of different designs and what problems they can cause during operation. Contact tests are carried out in several angular positions, and then the resulting contact pattern images are summarized to obtain a picture of the gear.

REFERENCES

[1] Pintér Ádám Sándor, Sarka Ferenc (2021). CAD rendszerek által generált fogazott elemek alakeltérésének vizsgálata. *GÉP*, 3–4, pp. 85–88., 4p.

[2] Sarka Ferenc (2019). Gördülőfelületek hordképvizsgálata. *Multidiszciplináris tudományok*, 1, pp. 172–177., 6p, https://doi.org/10.35925/j.multi.2019.1.22.

[3] Bodzás Sándor (2019). Designing and analysis of special gear pairs by gearteq and solidworks softwares. *7th International Scientific Conference on Advances in Mechanical Engineering (ISCAME 2019): Conference Proceedings (Book of Extended Abstracts)*, Department of Mechanical Engineering, Faculty of Engineering, University of Debrecen, http://real.mtak.hu/id/eprint/113657.

[4] Bodzás Sándor (2019). Hengeres fogaskerékhajtások tervezése és elemzése egyenes fogiránnyal. *Debreceni Szemle*, 27, 4, pp. 391–404., 14p. http://real.mtak.hu/id/eprint/113794.

[5] ANSI/AGMA 2001-D04: *Fundamental Rating Factors and Calculation Methods for Involute Spur and Helical Gear Teeth*.

[6] ISO 6336-3:2019. Calculation of load capacity of spur and helical gears. Part 3: Calculation of the benging strength

[7] Szabó, Ferenc János – Várkuliné Szarka, Ágnes (2019). Finite Element Study of Rotating Elements of a Ventilator. *International Review of Mechanical Engineering*, 13, 6, pp. 326–331., 6p, http://real.mtak.hu/id/eprint/113794.

[8] Szabó Ferenc János (2012). Veszélyes hibalehetőségek a végeselemes modellezés és optimálás során II. *GÉP*, 58, 12, pp. 121–126., 6p.

INVESTIGATION OF S960QL TYPE HIGH STRENGTH STEEL AND ITS WELDED JOINTS APPLYING ABSORBED SPECIFIC FRACTURE ENERGY AND NOTCH OPENING DISPLACEMENT

ILLÉS SAS[1] – JÁNOS LUKÁCS[2]

[1]*Elektro-MontőrING Ltd., Jászberény, Hungary*
[2]*Institute of Materials Science and Technology, Faculty of Mechanical Engineering and Informatics, University of Miskolc, Miskolc, Hungary*
[1]*sas@elektromontoring.hu*
[2]*janos.lukacs@uni-miskolc.hu*

Abstract: Classical techniques of fracture toughness evaluation, such as determination of the plain-strain fracture toughness, or the critical value of the crack-tip opening displacement are complex methods. The determination of the absorbed specific fracture energy and the notch opening displacement is basically simpler; notched cylindrical tensile specimens characterized by different notch radii can be applied. S960QL type high strength steel and its welded joints without and with preheating were examined; notch opening displacement and absorbed specific fracture energy values were determined. Conclusions belong to the effect of the preheating and the sensitivity of the high strength steel, as well as the reliability of the applied material characteristics were drawn.

Keywords: *high strength steel, cold cracking, notch opening displacement, absorbed specific fracture energy*

1. INTRODUCTION

The most commonly used structural material for the construction of engineering structures is (structural or low alloyed) steel, and the most widely used manufacturing technology is welding. Nowadays, steel producers develop modern versions of high strength base materials and filler metals with yield strength start from 690 MPa and up. However, high strength lightweight structures with low cost of steel weldments lead to apply in many practical aspects (e.g. mobile cranes, hydropower plants, offshore structures, trucks, earthmoving machines, and drums), because of an extensive reduction in weight [1].

The welded joints are sensitive parts of structures because the welded regions are in complex metallurgical state and stress condition. Before the Second World War, the design of all engineering structures was based on yield/tensile strength and ductility. Mild steel was used as the structural material and the minimum yield strength of the weld metal was found to be around 340 MPa. The yield strength to tensile strength ratio (Y/T) of the weld metals that were used for welding the mild steel in early designs was very high and the designers did not pay much attention to the yield

strength of the weld metals. It has been reported that the maximum yield strength of the filler metal that has been used for joining the mild steel plates was about 59% higher than the base material [2].

During the welding process, the joining parts are affected by heat and force, which cause inhomogeneous microstructure and mechanical properties, and further-more, stress concentrator places can form. Both the inhomogeneity of the welded joints and the weld imperfections play important role in case of different loading conditions. High cycle fatigue and fatigue crack growth phenomena are a very com-mon problem in welded structures [3], together cold cracking sensitivity, especially in high strength steels.

Classical techniques of fracture toughness evaluation, such as determination of the plain-strain fracture toughness (K_{Ic}), or the critical value of the crack(-tip) open-ing displacement (C(T)OD) are complex methods [4, 5]. The necessity of fracture mechanical test is inevitable, applying notched and precracked specimens [6]. The determination of the notch opening displacement (NOD) and/or the absorbed spe-cific fracture energy (ASPEF = W_c) is basically simpler; notched cylindrical tensile specimens can be applied, characterized by different notch radii.

The aims of our article are to introduce the notch opening displacement and the absorbed specific fracture energy quantities, and their application possibility at weld-ing of high strength steel and its welded joints.

2. BACKGROUND

It can be assumed that the ASPEF is the work of all external forces in an infinitesimal element in the crack point which is necessary for the propagation of crack. Thus the total energy is equal to the sum of energy of elastic deformation, energy of plastic deformation, and energy of crack propagation (formation of new fracture surface). The energy of elastic deformation will be released after the rupture; furthermore, the sur-face energy is negligible compared to the energy of plastic deformation. If we refer the energy of plastic deformation to the absorbing volume (V), we get a physically correct value. The ASPEF defined by the previous way can be determined applying tensile tests [7–9] (see *Figure 1* [10]), and can be calculated using *Equation (1)*:

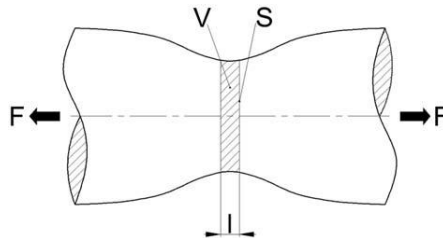$$W_c = \int_{l_0}^{l_u} \frac{F dl}{V} = \int_{0}^{\varphi_u} \sigma d\varphi \,. \tag{1}$$

Figure 1. *Characteristics of the un-notched and notched specimens* [10]

Figure 2 [10] shows a stress concentration place, in other words a notch, which can be considered a crack, if the notch radius is sufficiently small. Applying tensile stress, a plastic zone will formed in the root of the notch, in which considerable energy can be absorbed. The length (L) of the fictive tensile specimen is equal to the width of the plastic zone, and this length depends on the material characteristics and the sharpness of the notch. If we have crack the length value will be minimum, furthermore, the absorbed energy will be minimum, too. Regarding to the strain, the elongation (ΔL) depends on the material characteristics and the length (L), accordingly if we have crack the elongation will be minimum. This minimum value should be equal to the COD value. Both minimum values can be determined by indirect methods [11, 12].
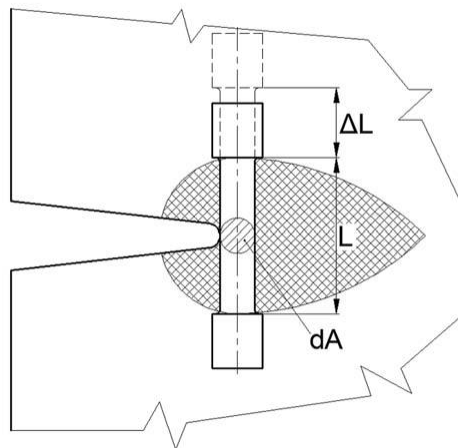

Figure 2

Stress concentration place with its plastic zone and fictive tensile specimen [10]

3. INVESTIGATIONS AND THEIR RESULTS

3.1. Preparation of welded joints

S960QL type, quenched and tempered high strength steel (produced by Thyssen Stahl AG and designated as XABO 960) was applied for our experiments. The chemical composition and the mechanical properties of the 15 mm thick base material plate can be found in *Table 1* and *Table 2*, respectively.

Table 1

Chemical composition of the used base material based on manufacturer certification (in weight%)

C	Si	Mn	P	S	Al	Cr	Mo	Ni	V
0.17	0.28	0.7	0.01	0.001	0.031	0.62	0.37	1.69	0.05

Table 2

Basic mechanical properties of the used base material based on manufacturer certification

Yield strength, R_{eH}, MPa	Tensile strength, R_m, MPa	Elon-gation, A, %	Charpy impact energy, KV, J				
			Testing temperature, °C	No1	No2	No3	Aver-age
1,003	1,077	15	–40°C	29	27	31	29
			–60°C	22	20	19	20

The dimensions of the welded workpieces were 600 mm x 125 mm. V joint shape was used, with 60° opening angle, with 2 mm gap between the two plates (root opening), and with 1 mm root face. The welding equipment was a MIG/MAG power source; 1.2 mm diameter solid wires in Union X96 (Böhler) types, and 18% CO_2 + 82% Ar gas mixture (M21) were applied. The welding position was flat position (PA).

Two welded joints were prepared, the first one without preheating, and the second one with preheating. Based on the chemical composition of the base material, the type of butt welded joint, and the applied welding process, the calculated preheating temperature was T_{pre} = 106 °C. Accordingly to the recommendation of the base material manufacturer, higher preheating temperature was selected, which was T_{pre} = 150 °C. It should be noted that during the preparation of the welded joint without preheating, the interpass temperature was less than T_{ip} = 50 °C. The welding technological parameters are summarized in *Table 3*. The table shows the welding current (I), the voltage (U), the wire-feed speed (v_{wire}) and the welding speed (v_w) values, with the heat input (Q). The parameters of the root and the filler layers were shown separately.

Table 3

The applied welding parameters during our experiments

Layer(s)	I, A	U, V	v_{wire}, m/min	v_w, mm/s	Q, kJ/mm
1 root	100–120	21–22	3.1–3.5	3.6–4.1	0.49–0.54
2–5 filler	240–275	29–31	10	9.2–13.0	0.49–0.72
6–10 filler	275–280	30–31	10	7.7–9.7	0.72–0.93

3.2. Basic investigation of welded joints

Welding procedure tests were accomplished on both welded joints; the detailed results of the non-destructive and mechanical tests can be found in *Table 4*.

<div align="right">*Table 4*</div>

Detailed results of the executed non-destructive and mechanical tests

Testing method	Welded joint without preheating	Welded joint with preheating (150 °C)
Visual testing (VT)	sufficient	sufficient
Magnetic particle testing (MT)	sufficient	sufficient
Ultrasonic testing (UT)	sufficient	sufficient
Tensile strength, R_m, MPa	1,011–1,037	1,013–1,047
Bending strain using non-standardized method with more rigorous criteria, %	38.1–38.3	38.2–38.4
Charpy impact energy in the weld metal at –40 °C, KV, J	48 (45–53)	51 (45–57)
Charpy impact energy in the heat affected zone at –40 °C, KV, J	54 (46–60)	63 (51–79)
Hardness, HV10	383–421	383–464

Comparing the results of the welded joints without preheating and with preheating, as well as the comparable results of the base material and the welded joints, it can be drawn that there are no significant differences between the results.

3.3. NOD and ASPEF investigations

Cylindrical notched specimens with different notch radii (R) were prepared to perform tensile tests. The different notch radii represent different stress concentration factors (K_t). *Figure 3* shows the characteristics of the un-notched and the notched specimens, where the diameter of the tested length of the un-notched specimens (d_0) and the minimum diameter of the notched specimens at the notches (d_0) were the same. The larger diameter (D_0) of the notched specimens was the same, too.

<div align="center">

Figure 3
Characteristics of the un-notched and notched specimens

</div>

Stress concentration factor (K_t) values were specified using a web calculator [13] developed based on formulas for stress and strain [14] and were controlled based on the well-known classical handbook [15]. The data belong to the specimens are summarized in *Table 5*.

<div align="right">*Table 5*</div>

<div align="center">*Characteristic data of the applied specimens*</div>

D_0, mm	d_0, mm	R, mm	d_0/D_0, –	R/D_0. –	K_t, –
N/A	4	∞	N/A	N/A	1
		1		0.167	1.67
		0.5		0.083	2.12
6	4	0.3	0.667	0.050	2.60
		0.2		0.033	3.07
		0.1		0.017	4.15

Notch Opening Displacement (NOD) investigations

Specimens cut from base material and welded joints without preheating and with preheating (150 °C) were investigated. The notch locations of the specimens cut from welded joints were different, namely located in the weld metal, or in the heat affected zone, or in the boundary of the joint parts. These different positions allowed a statistical evaluation of the properties of the welded joints.

To determine the notch opening displacement (NOD) values of the specimens, the contour lines of all different notch radii were projected before the tensile tests. After the tests, in other words after the rupture, the two broken parts of all specimens were fitted carefully and the changed contour lines were projected again. Using the differences between the two contour lines, the NOD values were determined. *Table 6* summarizes the results, the determined NOD values.

<div align="right">*Table 6*</div>

<div align="center">*The determined notch opening displacement (NOD) values (in mm)*</div>

R, mm	Base material	Welded joint without preheating	Welded joint with preheating (150 °C)
	0.35	0.72	N/A
1	0.50	0.66	N/A
	0.35	0.52	N/A
	N/A	N/A	0.57
0.5	N/A	N/A	0.42
	N/A	N/A	0.42
0.3	N/A	N/A	0.29
	0.29	0.25	0.25
0.2	0.28	0.31	0.28
	0.36	0.31	N/A
	0.29	0.22	0.18
0.1	0.22	0.36	0.17
	0.15	0.26	0.13

Based on the previously summarized theoretical background, there is a connection between the notch opening displacement (NOD) and the notch radius (R) values; and the value of the function at R = 0 (at crack) is equal to the crack opening displacement (COD), as follows:

$$NOD = kR + NOD_{R=0} = kR + COD \,.\tag{2}$$

Figure 4 shows the measured values and the regression lines using the Least Squares Fitting (LSF) method, taking into account all measured data can be found in *Table 6*.
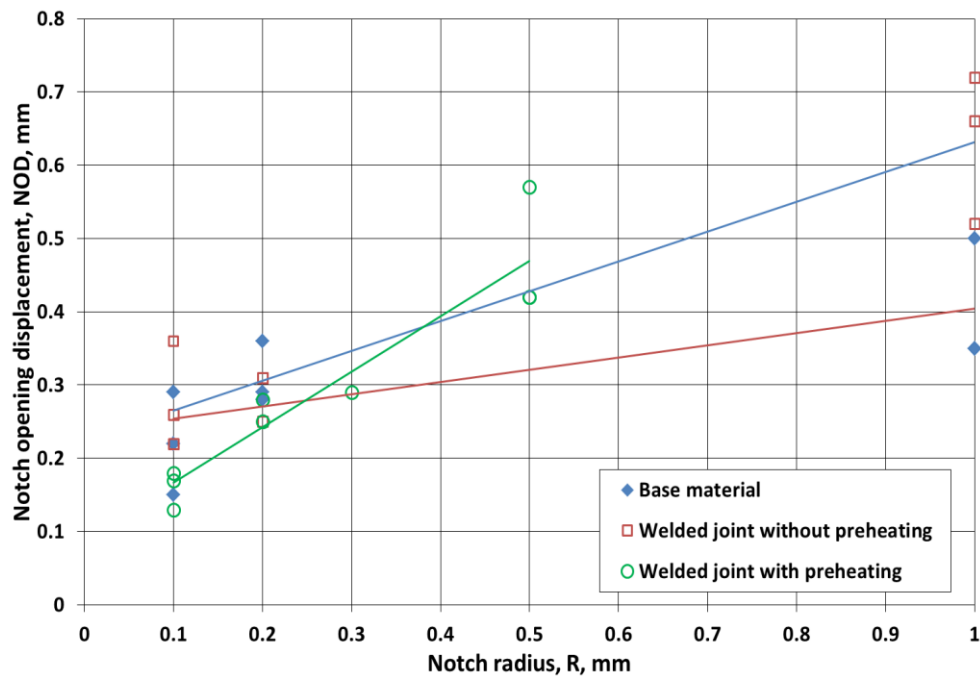

Figure 4
The NOD – R functions taking into account all measured data

Because the measured notch opening displacement (NOD) values belong to different notch radii (R) in the three main groups (base material and welded joints), and there are different number of specimens at notch radii, mathematical-statistical values of the samples (NOD values at notch radius) were calculated. Using the average NOD values, NOD – R functions were imaged. The calculated average, standard deviation (STD) and standard deviation coefficient values can be found in *Table 7*, and the NOD – R functions taking into account the average values of the measured data can be seen in *Figure 5*.

The main statistical parameters of the investigated NOD samples

| R, mm	Statistical parameter	Base material	Welded joint without preheating	Welded joint with preheating (150 °C)
1	Average	0.400	0.633	N/A
	STD	0.087	0.103	N/A
	STD coefficient	0.217	0.162	N/A
0.5	Average	N/A	N/A	0.470
	STD	N/A	N/A	0.087
	STD coefficient	N/A	N/A	0.184
0.3	N/A	N/A	N/A	N/A
0.2	Average	0.310	0.290	0.265
	STD	0.044	0.035	N/A
	STD coefficient	0.141	0.119	N/A
0.1	Average	0.220	0.280	0.160
	STD	0.070	0.072	0.026
	STD coefficient	0.318	0.258	0.165
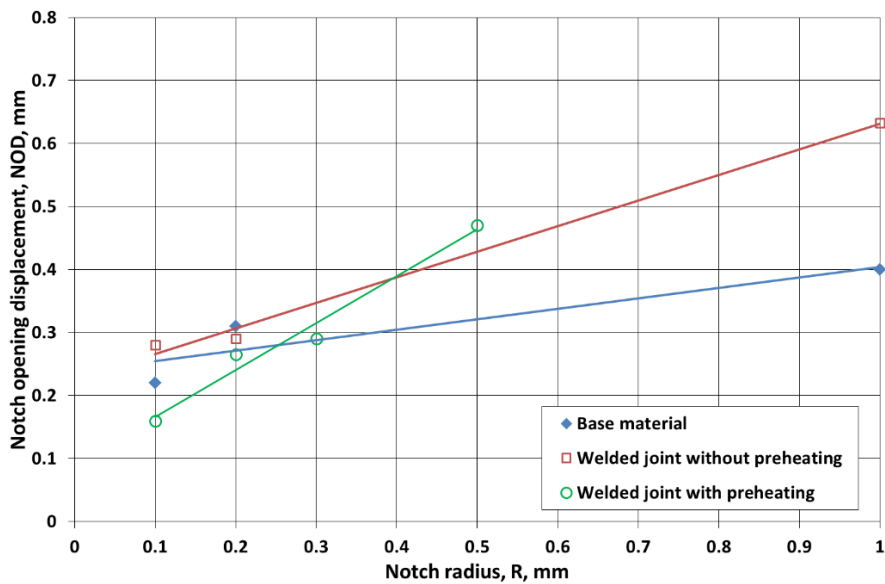
Figure 5
The NOD – R functions taking into account the average values
of the measured data

Table 8 summarizes the calculated slope (k), COD (NOD$_{R = 0}$) and correlation coefficient values of the approximated straight lines of the three groups, belonging to both all data and average values.

Table 8

The regression parameters of the NOD – R functions and the correlation coefficient values

Group	Material / welded joint	k	NOD$_{R = 0}$ = COD, mm	Correlation coefficient
All data	Base material	0.407	0.225	0.9354
	Welded joint without preheating	0.166	0.238	0.7238
	Welded joint with preheating (150 °C)	0.756	0.091	0.9413
Average value	Base material	0.166	0.238	0.9122
	Welded joint without preheating	0.406	0.225	0.9970
	Welded joint with preheating (150 °C)	0.744	0.092	0.9869

Correlation coefficient values demonstrate clearly that using the average values the results are more reliable than using all data.

Absorbed Specific Fracture Energy (ASPEF) investigations

The absorbed specific fracture energy values (W_c) were calculated using the load – extension diagrams and the geometrical features of the specimens. Tensile strength (R_m) and fracture strength (R'_u) values were calculated based on the appropriate loads (F_m and F_u, respectively) and specimen diameters (d_0 and d_u, respectively), where the following equation was applied:

$$W_c = \left(\frac{R_m + R'_u}{2}\right) 2 ln \left(\frac{d_0}{d_u}\right). \tag{3}$$

Table 9 summarizes the results, the determined W_c values, furthermore, the calculated statistical parameters can be found in *Table 10*.

Table 9

The determined absorbed specific fracture energy (W_c) values (in MJ/m^3)

R, mm	K$_t$, –	Base material	Welded joint without preheating	Welded joint with preheating (150 °C)
∞	1	2,210	871	1,598
		2,243	1,513	1,573
		2,232	1,352	1,636
1	1.67	505	673	N/A
		753	747	N/A

R, mm	K_t, –	Base material	Welded joint without preheating	Welded joint with preheating (150 °C)
		450	586	N/A
		N/A	N/A	681
0.5	2.12	N/A	N/A	621
		N/A	N/A	636
0.3	2.60	N/A	N/A	467
		462	293	281
0.2	3.07	396	253	346
		338	281	N/A
		319	269	158
0.1	4.15	319	216	246
		241	325	124

Table 10

The main statistical parameters of the investigated W_c samples

R, mm	Statistical parameter	Base material	Welded joint without preheating	Welded joint with preheating (150 °C)
∞	Average	2,228	1,245	1,602
	STD	16.8	334.0	31.7
	STD coefficient	0.0075	0.2682	0.0198
1	Average	569	669	N/A
	STD	161.4	80.6	N/A
	STD coefficient	0.2835	0.1205	N/A
0.5	Average	N/A	N/A	646
	STD	N/A	N/A	31.2
	STD coefficient	N/A	N/A	0.0483
0.3	N/A	N/A	N/A	N/A
0.2	Average	399	276	314
	STD	62.0	20.5	N/A
	STD coefficient	0.1556	0.0745	N/A
0.1	Average	293	270	176
	STD	45.0	54.5	63.0
	STD coefficient	0.1537	0.2019	0.3577

For analogous reasons to those described under the NOD investigations, both all W_c data and average W_c data were illustrated in *Figure 6* and *Figure 7*, respectively.
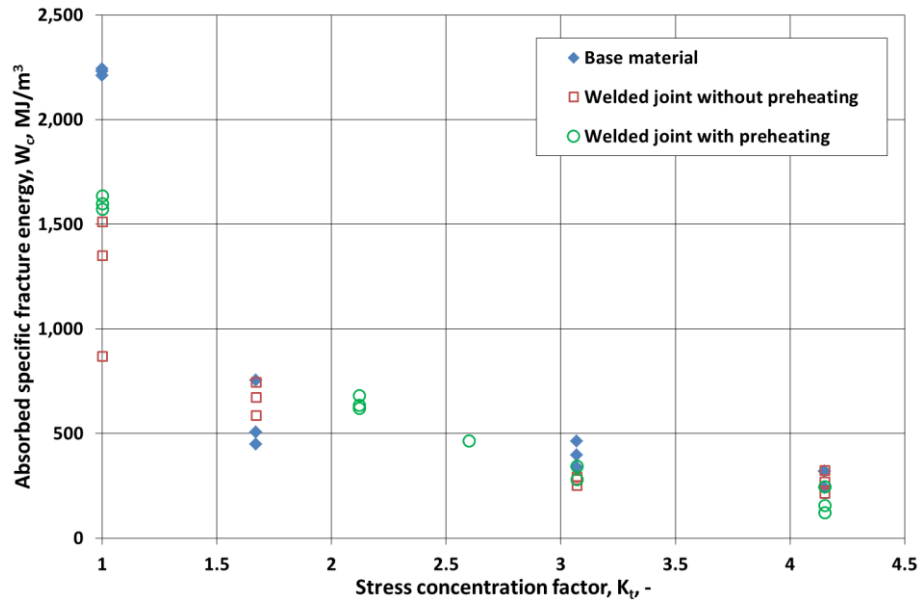
Figure 6
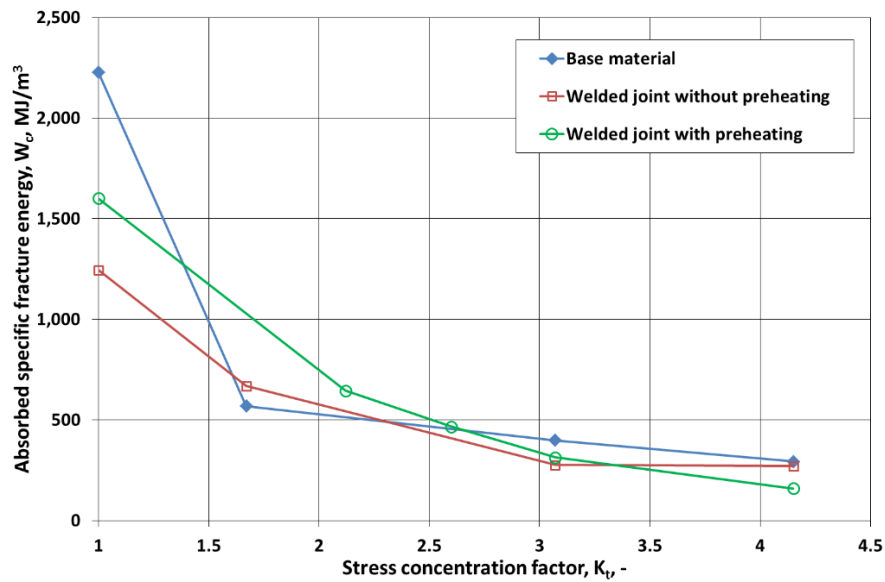*The W_c – K_t functions taking into account all measured data*

Figure 7
The W_c – K_t functions taking into account the average values of the measured data

4. SUMMARY AND CONCLUSIONS

Based on our investigations and the calculated results, the following findings and conclusions can be drawn.

The applied gas metal arc welding process and technological parameters are suitable for production welded joints of the investigated high strength steel with eligible quality.

Based on the executed welding procedure tests and their results, the applied preheating temperature has no significant effect on the main characteristics (imperfections and mechanical properties) of the welded joint.

Applying the notch opening displacement (NOD) and the absorbed specific fracture energy (W_c) values, both the base material and the welded joints without and with preheating can be characterised from other point of view (in our case cold cracking sensitivity), too.

Because of different notch radii (R) were applied in the three main groups (base material and welded joints), and different number of specimens were investigated at different notch radii, it was necessary analysing both all measured data and calculated average data. Both the notch opening displacement (NOD) and the absorbed specific fracture energy (W_c) samples consists of relatively small number of data (in other words specimens), in several cases have high standard deviation coefficients. (See grey coloured cells in *Table 7* and *Table 10*.) During the further investigations, the element number of samples (in other words the number of the tested specimens) should be increased.

Based on notch opening displacement (NOD) and absorbed specific fracture energy (W_c) investigations, and based on both all data and average data, the applied preheating temperature has no significant effect on NOD and W_c values, in other approach on cold crack sensitivity of the welded joints. Only COD ($NOD_{R=0}$) value of the preheated welded joint is an exception, however that is a consequence of the applied notch radii. It should be noted that the investigated welded joints were prepared without constraints; the deformations of the welded plates were free during the welding process. In that case when the welded structure can be produced without constraints, further investigations should be accomplished to study the welding technology without preheating temperature. In that case when the welded structure can be only produced with constraints, further investigations should be accomplished to study the determination of the efficient preheating temperature. These investigations can be built upon notch opening displacement (NOD) and absorbed specific fracture energy (W_c).

REFERENCES

[1] Ravi, S. – Balasubramanian, V. – Nemat Nasser, S. (2004). Effect of mismatch ratio (MMR) on fatigue crack growth behaviour of HSLA steel welds. *Engineering Failure Analysis*, Vol. 11, No. 3, pp. 413–428, June 2004. https://doi.org/10.1016/j.engfailanal.2003.05.013

[2] Mobark, H. F. H. – Lukács, J. (2018). Mismatch effect influence on the high cycle fatigue resistance of S690QL type high strength steels. *2nd International Conference on Structural Integrity and Durability*, Dubrovnik, Croatia, October 2–5.

[3] Schroepfer, D. – Kannengiesser, T. (2016). Stress build-up in HSLA steel welds due to material behaviour. *Journal of Materials Processing Technology*, Vol. 227, pp. 49–58, https://doi.org/10.1016/j.jmatprotec.2015.08.003.

[4] ISO 12135:2016. Metallic materials – Unified method of test for the determination of quasistatic fracture toughness, 2016.

[5] ISO 15653: 2018.Metallic materials – Method of test for the determination of quasistatic fracture toughness of welds, 2018.

[6] Koncsik, Zs. (2019). Lifetime analyses of S960M steel grade applying fatigue and fracture mechanical approaches. In: Szita Tóthné, K. – Jármai, K. – Voith, K. (eds.). *Solutions for Sustainable Development: Proceedings of the 1st International Conference on Engineering Solutions for Sustainable Development (ICESSD 2019)*, October 3–4, Miskolc, Hungary, CRC Press, pp. 316–324, https://doi.org/10.1201/9780367824037.

[7] Gillemot, L. (1961). Zur rechnerischen Ermittlung der Brucharbeit. *Materialprüfung*, Vol. 3, No 9, pp. 330–336, https://doi.org/10.1515/mt-1961-030902.

[8] Gillemot, L. (1964). Eine neue method zur Bestimmung der Sprödbruchgefahr. *Periodica Polytechnica Mechanical Engineering*, Vol. 8, No. 1, pp. 1–14.

[9] Gillemot, L. (1976). Criterion of crack initiation and spreading. *Engineering Fracture Mechanics*, Vol. 8, pp. 239–253. https://doi.org/10.1016/0013-7944(76)90089-8

[10] Czoboly, E. – Havas, I. – Orbulov, I. (2012). Törési vizsgálatok a BME Mechanikai Technológia Tanszéken. *Anyagvizsgálók Lapja*, Válogatás 2012 – Jubileumi szám, pp. 43–45.

[11] Gillemot, L. – Czoboly, E. (1970). Generalized Theory of Fracture. *II. Conference on Brittle Fracture*, Marianske Lázne, No. 11, pp.1–21.

[12] Czoboly, E. – Havas, I. – Gillemot, F. (1981). The absorbed specific energy till fracture as a measure of the toughness of metals. In: Sih, G. C. – Czoboly, E. – Gillemot, F. (eds.). *Proceedings of International Symposium on Absorbed Specific Energy and/or Strain Energy Density Criterion*. Sijthoff and Noordhoff International Publishers, Alphen aan den Rijn, pp. 107–130.

[13]   https://amesweb.info/stress-concentration-factor-calculator/u-groove.aspx.

[14]   Pilkey, W. D. (2005). *Formulas for Stress, Strain, and Structural Matrices*.
       2nd Edition, John Wiley & Sons, Inc., Hoboken, NJ.
       https://doi.org/10.1002/9780470172681.

[15]   Pikley, W. D. (1997). *Peterson's Stress Concentration Factors*. 2nd
       Edition, John Wiley & Sons, Inc., New York/Chichester/Weinheim /
       Brisbane / Singapore / Toronto.

REVIEWING COMMITTEE